

# A mimetic finite difference based quasi-static magnetohydrodynamic solver for force-free plasmas in tokamak disruptions

Zakariae Jorti<sup>a,1</sup>, Qi Tang<sup>a,1</sup>, Konstantin Lipnikov<sup>a,1</sup>, Xian-Zhu Tang<sup>a,1</sup>

<sup>a</sup>*Theoretical Division, Los Alamos National Laboratory, Los Alamos, 87545, New Mexico, U.S.A.*

---

## Abstract

Force-free plasmas are a good approximation where the plasma pressure is tiny compared with the magnetic pressure, which is the case during the cold vertical displacement event (VDE) of a major disruption in a tokamak. On time scales long compared with the transit time of Alfvén waves, the evolution of a force-free plasma is most efficiently described by the quasi-static magnetohydrodynamic (MHD) model, which ignores the plasma inertia. Here we consider a regularized quasi-static MHD model for force-free plasmas in tokamak disruptions and propose a mimetic finite difference (MFD) algorithm. The full geometry of an ITER-like tokamak reactor is treated, with a blanket module region, a vacuum vessel region, and the plasma region. Specifically, we develop a parallel, fully implicit, and scalable MFD solver based on PETSc and its DMStag data structure for the discretization of the five-field quasi-static perpendicular plasma dynamics model on a 3D structured mesh. The MFD spatial discretization is coupled with a fully implicit DIRK scheme. The algorithm exactly preserves the divergence-free condition of the magnetic field under the resistive Ohm's law. The preconditioner employed is a four-level fieldsplit preconditioner, which is created by combining separate preconditioners for individual fields, that calls multigrid or direct solvers for sub-blocks or exact factorization on the separate fields. The numerical results confirm the divergence-free constraint is strongly satisfied and demonstrate the performance of the fieldsplit preconditioner and overall algorithm. The simulation of ITER VDE cases over the actual plasma current diffusion time is also presented.

*Keywords:* Magnetohydrodynamics, Mimetic finite difference, Staggered structured grid, Fully implicit algorithms, JFNK

---

<sup>1</sup>This work was jointly supported by the U.S. Department of Energy through the Fusion Theory Program of the Office of Fusion Energy Sciences and the SciDAC partnership on Tokamak Disruption Simulation between the Office of Fusion Energy Sciences and the Office of Advanced Scientific Computing. It was also partially supported by Mathematical Multifaceted Integrated Capability Center (MMICC) of Advanced Scientific Computing Research. Los Alamos National Laboratory is operated by Triad National Security, LLC, for the National Nuclear Security Administration of U.S. Department of Energy (Contract No. 89233218CNA000001).

## Contents

<b>1</b>	<b>Introduction</b>	<b>2</b>
<b>2</b>	<b>Quasi-static force-free MHD model</b>	<b>5</b>
2.1	Regularized quasi-static force-free model . . . . .	5
2.2	Coupling to ITER blankets and vacuum vessel . . . . .	8
2.3	Quasi-static perpendicular plasma dynamics model and its interface conditions . . . . .	9
<b>3</b>	<b>Mimetic finite difference discretization</b>	<b>10</b>
3.1	Primary and derived mimetic operators . . . . .	11
3.2	MFD discretization of the quasi-static perpendicular plasma dynamics model . . . . .	12
<b>4</b>	<b>Solver and preconditioning strategy</b>	<b>16</b>
<b>5</b>	<b>Numerical results</b>	<b>19</b>
5.1	Computing the effective resistivity of ITER vacuum vessel . . . . .	19
5.2	Preparing the initial state for the quasi-static force-free model . . . . .	22
5.3	Comparing the different regularizations . . . . .	24
5.4	Full cold ITER VDE simulation . . . . .	27
5.4.1	Isotropic setting . . . . .	28
5.4.2	Anisotropic setting . . . . .	30
5.5	Solver performance . . . . .	31
<b>6</b>	<b>Conclusions</b>	<b>33</b>
<b>Appendix A</b>	<b>Nonuniqueness of solutions to the model without the viscosity term</b>	<b>34</b>
<b>Appendix B</b>	<b>Regularization through the viscosity term</b>	<b>37</b>
<b>Appendix C</b>	<b>Matrix definition of the derived mimetic operators</b>	<b>37</b>
<b>Appendix D</b>	<b>Magnetic energy dissipation</b>	<b>38</b>

## 1. Introduction

The macroscopic plasma motion can be described by the plasma momentum equation in the magnetohydrodynamic (MHD) model [1]

$$\rho \left( \frac{\partial \mathbf{V}}{\partial t} + \mathbf{V} \cdot \nabla \mathbf{V} \right) = \mathbf{j} \times \mathbf{B} - \nabla p - \nabla \cdot \boldsymbol{\pi}, \quad (1)$$

where  $\rho$  is the plasma mass density,  $\mathbf{V}$  the flow field,  $p$  the plasma pressure,  $\boldsymbol{\pi}$  the viscosity tensor,  $\mathbf{j} \times \mathbf{B}$  the Lorentz force with  $\mathbf{B}$  the magnetic field, and  $\mu_0 \mathbf{j} = \nabla \times \mathbf{B}$  the plasma current with  $\mu_0$  the vacuum magnetic permeability. A large class of practical problems considers low-beta plasmas in which the plasma pressure is low compared with the magnetic pressure. The limiting case is  $\nabla p \approx 0$ , so after a possible transient period over which the plasma flow is damped by viscosity, the plasma will settle into a steady state that is approximately force-free,

$$\mathbf{j} \times \mathbf{B} = 0, \quad (2)$$

and  $\mathbf{V} \approx 0$  (hence  $\boldsymbol{\pi} \approx 0$ ). This is a *force-free plasma* where the plasma current supports a force-free magnetic field satisfying Eq. (2). The general solution to Eq. (2) is [2]

$$\mathbf{j} = \lambda \mathbf{B}. \quad (3)$$

A quasi-neutral plasma has  $\nabla \cdot \mathbf{j} = 0$ . Combining this constraint with Eq. (3), and making use of  $\nabla \cdot \mathbf{B} = 0$ , one finds

$$\mathbf{B} \cdot \nabla \lambda = 0, \quad (4)$$

which says that  $\lambda$  is a constant along a magnetic field line. If the magnetic field is integrable with an irrational winding number [3],  $\lambda$  will be a function of the flux surface label  $\psi$ , i.e.,  $\lambda(\psi)$ . This can be the case in which the magnetic field obeys geometrical symmetry, say the toroidal symmetry in a tokamak. For a three-dimensional magnetic field with no geometrical symmetry, the magnetic field line is generally non-integrable, so the stochastic field line fills an ergodic sub-volume in space, for which Eq. (4) implies a constant  $\lambda$ . If the magnetic field produces globally stochastic field lines, one would have  $\lambda$  a global constant.

It is of interest to note that  $\mathbf{j} = \lambda \mathbf{B}$  with  $\lambda$  a global constant is the celebrated Taylor state, which is the minimum energy state for a zero-beta plasma under the constraint of conserved magnetic helicity [4, 5, 6]. The connection between magnetic field line topology and  $\lambda$  indeed underlies the dynamical processes by which the so-called magnetic or Taylor relaxation is realized (see Ref. [7] for instance). Namely, when the plasma becomes unstable to macroscopic MHD instabilities, flux surfaces would be broken so that the magnetic field lines can become globally stochastic, which then relax  $\lambda$  to be a global constant. For weak stochasticity, even small perpendicular current associated with the plasma inertia, can produce significant modulation in  $\lambda$  along the magnetic field line due to the Pfirsch-Schlüter effect [8]. As the MHD instabilities die down and the flux surfaces reheel, like those in laboratory confinement experiments with reversed field pinch [9], spheromaks [10], spherical tokamak [11, 12, 13], and tokamak disruptions [14], or in the solar corona [15] and radio lobes [16], one can end up with a force-free plasma with  $\lambda(\psi)$  a function of the flux surface label  $\psi$ , also known as a nonlinear force-free magnetic field [17, 18, 19, 20], which despite the deviation from the constant  $\lambda$  Taylor state, retains the key feature of magnetic self-organization via a resonant coupling between the helicity injection source and global magnetic configuration [21, 22, 23]. Further evolution of such a nonlinear force-free plasma, for example, a post-thermal-quench tokamak plasma undergoing a cold vertical displacement event (VDE), is governed by the slow transport process, namely the resistive decay of the plasma current. By slow, we refer to a time scale much longer than the transit time of the Alfvén waves, which sets the time scale for the zero-beta plasma to re-establish force-balance. This condition is easily satisfied in a plasma with Lundquist number much greater than unity, which applies to most cases of practical interest. It is of interest to note that during the cold VDE after the plasma thermal quench, the Ohmic heating power by a decaying plasma current, is mostly balanced by radiative cooling, so the zero-beta or force-free plasma remains a good approximation throughout the VDE [24].

The drastic time scale separation between Ohmic decay of the plasma current and re-establishment of force-balance in a zero-beta plasma by Alfvén waves, suggests the utility of a quasi-static force-free description of the plasma dynamics on transport time scale as opposed to the full Alfvén wave dynamics. The most obvious and naive form is

$$(\nabla \times \mathbf{B}) \times \mathbf{B} = 0 \quad (5)$$

$$\frac{\partial \mathbf{B}}{\partial t} = -\nabla \times \mathbf{E} \quad (6)$$

$$\mathbf{E} = -\mathbf{V} \times \mathbf{B} + \frac{\eta}{\mu_0} \nabla \times \mathbf{B} \quad (7)$$

with  $\eta$  the plasma resistivity. As shown later in [Appendix A](#) as well as by many others (see [\[25\]](#) for detailed discussions on force-free fields in astrophysics), this model however is not well posed without a proper regularization. The solution to such a quasi-static model has long benefited from a MHD relaxation method that Chodura and Schlüter first introduced to find a 3D MHD equilibrium [\[26\]](#). The idea is to introduce a fictitious drag coefficient  $\epsilon$  so the force-balance equation is regularized as

$$\epsilon \mathbf{V} = \frac{1}{\mu_0} (\nabla \times \mathbf{B}) \times \mathbf{B} - \nabla p. \quad (8)$$

This is to be solved in combination with the induction equation and the ideal Ohm's law

$$\frac{\partial \mathbf{B}}{\partial t} = -\nabla \times \mathbf{E} \quad (9)$$

$$\mathbf{E} = -\mathbf{V} \times \mathbf{B} \quad (10)$$

and the constraint  $\nabla \cdot \mathbf{B} = 0$ . Setting  $\nabla p = 0$  would recover the force-free magnetic field as  $\mathbf{V}$  is damped to zero by the fictitious drag toward a steady state. This ends up to be a popular numerical model for studying force-free coronal magnetic fields in solar physics. [\[27, 28, 29, 30\]](#)

Recent interests in the quasi-static MHD model for magnetic confinement fusion have focused on the tokamak disruption modeling, particularly the force-free evolution of a cold VDE after the initial thermal quench. The basic physics is that once the thermal quench drives the plasma beta to approximately zero, the vertical force-balance of the plasma column is lost on the time scale that the vertical position control coil current can be adjusted to provide the counter-acting vertical magnetic fields. The vertical displacement of the entire current-carrying plasma column is driven by the Ohmic current decay rate, the physics of which is described by a finite  $\eta$  in [Eq. \(7\)](#). This is a problem quite amendable for a quasi-static treatment, and the MHD relaxation method of Chodura and Schlüter has been employed by replacing [Eq. \(5\)](#) with [Eq. \(8\)](#) in [Ref. \[31\]](#) and [\[32\]](#).

Here we revisit the formulation of the quasi-static force-free MHD model and its numerical solution by implicit time stepping. Specifically we will analyze the role of the fictitious drag force in the regularization of the model and its physical implication on the solution. This will be followed by proposing an alternative regularization of the model, which we find to have a more straightforward physics interpretation. In terms of spatial discretization, a focus is on ensuring the divergence-free constraint of the magnetic field, as failure to do so is known to spoil the numerical solution [\[33, 34\]](#). Various approaches have been proposed in the literature, such as starting from existing convergent discretizations and enhancing their numerical accuracy by introducing appropriate divergence-free reconstructions [\[35\]](#), or employing divergence-free methods, like divergence-free Discontinuous Galerkin methods [\[36\]](#), and stable finite element method [\[37\]](#). A particularly relevant and common approach in the compressible MHD literature is the constrained transport approach originally proposed in [\[38\]](#), where a staggered formulation of the electric and magnetic fields is proposed to create specific mimetic finite difference operators that result in a magnetic field which is divergence-free regarding a specific discrete divergence operator. The recent work attempts to generalize it to a non-staggered formulation such as finite volume [\[39\]](#), high-order finite difference [\[40, 41\]](#), and the extension to a mapped curvilinear grid [\[42\]](#). There also exists abundant literature on spatial discretizations for the MHD equations, see [\[43, 44, 45, 46, 47, 48\]](#) and the references therein.

For the linear solver part, there has been a lot of research work focusing on the design of efficient and scalable preconditioners for solving linear systems stemming from MHD models. [Ref. \[49\]](#) proposes scalable block preconditioners for Newton-Krylov solver that rely on the approximate block factorization (ABF) approach and the recursive approximation of the Schur complement.

Ref. [50, 48] follow the same line of thinking by employing the physical-based ABF technique to devise a preconditioner for fully-implicit Newton-Krylov solvers. By expressing the matrix in blocks corresponding to different unknowns, and approximating the resulting Schur complements, they carry out a parabolization which transforms ill-conditioned hyperbolic systems that are difficult to solve into well-conditioned diagonally dominant parabolic operators for which multigrid (MG) methods perform very well. More recently, a new family of recursive block LU preconditioners is proposed in [51] for solving the thermally coupled inductionless MHD equations, whereas in [52] robust block preconditioners, which satisfy the divergence-free condition exactly when used in Krylov iterative methods, are developed for the structure-preserving discretization of the incompressible MHD system.

In this paper, we use a Mimetic Finite Difference (MFD) method [53] for the discretization of a quasi-static perpendicular plasma dynamics model on a 3D structured grid. There is a rich literature on the usage of this method for solving diffusion [54], advection-diffusion [55, 56], elasticity [57], Stokes [58] and porous media flow problems [59]. As for the time-integration, we use a fully implicit L-stable second order diagonally implicit Runge-Kutta (DIRK) scheme [60]. The preconditioner employed in this article is a four-level block preconditioner, which is created by combining separate preconditioners for individual fields (as many splits as fields), that calls multigrid methods or exact factorization on the separate fields.

The rest of this article is structured as follows. Section 2 introduces the quasi-static perpendicular plasma dynamics model. Section 3 presents some basic elements of the mimetic discretization methodology and presents the discrete equations of the quasi-static model. The numerical results of the mimetic finite difference method applied to the quasi-static perpendicular plasma dynamics model are shown in Section 5. It is followed by the conclusion section of Section 6. Some mathematical aspects of the models, such as well-posedness and the energy dissipation law, are included in the appendix.

## 2. Quasi-static force-free MHD model

### 2.1. Regularized quasi-static force-free model

The concept of a quasi-static force-free MHD model is based upon the idea that any force imbalance introduced by the resistive decay of plasma current in the Ohm's law of Eq. (6), is quickly removed by the Alfvén wave dynamics, so at any given instance, the plasma is approximately in a force-free state. By dropping the plasma inertia in Eq. (5), the Alfvén wave dynamics is deliberately removed, so maintaining a force-free magnetic field comes from the solution of the perpendicular flow

$$\mathbf{V}_\perp \equiv \mathbf{V} - \mathbf{V} \cdot \mathbf{B} / |\mathbf{B}| \quad (11)$$

from Eq. (7), subjected to the force-free constraint of Eq. (5). The Faraday's law, Eq. (6), connects the constraint of Eq. (5) to the solution of  $\mathbf{V}_\perp$  from Eq. (7). In other words, the Ohm's law is the equation from which  $\mathbf{V}_\perp$  is solved. One obvious implication of this is that since this is a time-dependent partial differential equation with a constraint, one would need to solve the time-dependent equations with implicit time stepping.

A more subtle implication, although well-known in the constrained optimization problem such as saddle point problems [61, 62], is the need for regularization. In the specific case of the quasi-static force-free MHD model, the coupled system of Eqs. (5, 6, 7) has a null space in the solution of  $\mathbf{V}_\perp$ . One can see this by noting that if  $\mathbf{V}_\perp$  is a solution, then  $\mathbf{V}_\perp + \delta\mathbf{V}_\perp$  is also a solution with

$$\delta\mathbf{V}_\perp = -\frac{\nabla\varphi \times \mathbf{B}}{B^2} \quad (12)$$

for any  $\varphi$  that satisfies

$$\mathbf{B} \cdot \nabla \varphi = 0. \quad (13)$$

The underlying physics is that the electrostatic field, which can be written as  $-\nabla\varphi$ , does not contribute to  $\nabla \times \mathbf{E}$  and hence has no effect on magnetic field evolution. This results in a degeneracy of the mathematical formulation that cannot be inverted for  $\mathbf{V}_\perp$  that is required in quasi-static evolution. The formal derivation of such a null space is given in [Appendix A](#).

To gain insights into how the degeneracy can be removed, we introduce an explicit treatment of the electrostatic potential  $\Phi$  via a Helmholtz decomposition of the electric field,

$$\mathbf{E} = -\nabla\Phi + \nabla \times \mathbf{h} = -\nabla\Phi + \boldsymbol{\tau}. \quad (14)$$

Substituting this form of  $\mathbf{E}$  into Eq. (7), we find

$$\boldsymbol{\tau} = \nabla\Phi - \mathbf{V}_\perp \times \mathbf{B} + \frac{\eta}{\mu_0} \nabla \times \mathbf{B}. \quad (15)$$

The Faraday's law, Eq. (6), is now rewritten as

$$\frac{\partial \mathbf{B}}{\partial t} = -\nabla \times \boldsymbol{\tau}. \quad (16)$$

The final step is to come up with another equation to solve for  $\Phi$ , which can be done in the usual way by taking the divergence of the electric field,

$$\nabla^2 \Phi = -\nabla \cdot \left[ -\mathbf{V}_\perp \times \mathbf{B} + \frac{\eta}{\mu_0} \nabla \times \mathbf{B} \right] \quad (17)$$

The boundary condition for  $\Phi$ , in the case of ITER configuration, is simply

$$\Phi|_{\partial\Omega} = 0, \quad (18)$$

where the boundary  $\partial\Omega$  is the outer vacuum vessel wall, which is assumed to be perfectly conducting on the time scale of a major disruption. So in all, we add one more unknown ( $\Phi$ ) and one additional equation, Eq. (17), with its boundary condition, Eq. (18), to the quasi-static force-free model.

A special null space in an axisymmetric tokamak plasma is particularly relevant. For an axisymmetric tokamak plasma with flux surface label  $\psi$ , a pure radial electric field

$$\mathbf{E} = -\nabla\varphi(\psi) = -\frac{\partial\varphi}{\partial\psi} \nabla\psi \quad (19)$$

is unconstrained by Eq. (17). To see this, one can substitute  $\mathbf{V}_\perp + \delta\mathbf{V}_\perp$  with  $\delta\mathbf{V}_\perp$  given in Eq. (12) having  $\varphi = \varphi(\psi)$ , for  $\mathbf{V}_\perp$  in Eq. (15) and Eq. (17). The result is

$$\boldsymbol{\tau} = \nabla(\Phi - \varphi(\psi)) - \mathbf{V}_\perp \times \mathbf{B} + \frac{\eta}{\mu_0} \nabla \times \mathbf{B} \quad (20)$$

$$\nabla^2(\Phi - \varphi(\psi)) = -\nabla \cdot \left[ -\mathbf{V}_\perp \times \mathbf{B} + \frac{\eta}{\mu_0} \nabla \times \mathbf{B} \right], \quad (21)$$

which says that  $\Phi - \varphi(\psi)$  is also a solution if  $\Phi$  is a solution. This null space for the solution of  $\mathbf{V}_\perp$  or degeneracy of the force-free model with respect to a pure radial electric field of the form in Eq. (19) needs to be removed for numerical computation. The fictitious viscous drag in

Eq. (8), first introduced by Chodura and Schlüter [26], precisely provides such a regularization. Specifically the value of the fictitious viscous drag coefficient  $\epsilon$  picks a particular  $\varphi(\psi)$ . In other words, the regularization of the quasi-static force-free model sets a radial electrical field that is not constrained by the MHD model. Although this peculiarity does not affect the force-free magnetic field during the quasi-static evolution, one needs to be aware of the regularization-induced radial electric field  $\varphi(\psi)$ . For example, should one be interested in advancing the particle motion using the electromagnetic field from this regularized quasi-static model, the component of the pure radial electric field should be removed as it is not *physically* constrained in the MHD model.

This artificialness in radial electric field motivates a more careful look at the widely used  $\epsilon\mathbf{V}$  regularization approach. The physical origin of the collisional damping of the flow field in single fluid MHD, which is to be mimicked by  $\epsilon\mathbf{V}$ , is not collisional friction, but the viscosity in Eq. (1). This suggests that a more physically sound regularization is to simply retain the viscosity while ignoring the inertia, so

$$(\nabla \times \mathbf{B}) \times \mathbf{B} = -\mu_0 \nabla \cdot \boldsymbol{\pi}. \quad (22)$$

For simplicity, we adopt the approximate form

$$\nabla \cdot \boldsymbol{\pi} = \nu \nabla^2 \mathbf{V}, \quad (23)$$

so the alternatively regularized force-free constraint is

$$(\nabla \times \mathbf{B}) \times \mathbf{B} = -\mu_0 \nu \nabla^2 \mathbf{V}. \quad (24)$$

The formal derivation of the regularization term removing the null space is given in [Appendix B](#). In addition, note that an energy dissipation law can be derived with this regularization term, see the derivation in [Appendix D](#). If one desires, part of the plasma inertia, which is quadratic in  $\mathbf{V}$ , can be retained as well,

$$(\nabla \times \mathbf{B}) \times \mathbf{B} = \mu_0 \nu \nabla^2 \mathbf{V} + \rho \mathbf{V} \cdot \nabla \mathbf{V}. \quad (25)$$

For  $\mathbf{V}$  with small amplitude, which scales with  $\eta$ , the quadratic inertia term has very little effect. Finally, we should note that the force-free MHD model does not constrain  $\mathbf{V} \cdot \mathbf{B}$  at all, the regularized quasi-static force-free MHD model is supplemented with the constraint,

$$\mathbf{B} \cdot \mathbf{V} = 0. \quad (26)$$

In summary, we consider two forms of regularized quasi-static force-free MHD model in the current work. One uses the fictitious drag of Chodura and Schlüter for regularization,

$$(\nabla \times \mathbf{B}) \times \mathbf{B} = \epsilon \mathbf{V}, \quad (27)$$

while the other invokes the viscous damping regularization, Eq. (24) or Eq. (25). One of these regularized force-balance equations (24, 25, 27) will be solved in tandem with

$$\frac{\partial \mathbf{B}}{\partial t} = -\nabla \times \boldsymbol{\tau}, \quad (28)$$

$$\boldsymbol{\tau} = \nabla \Phi - \mathbf{V} \times \mathbf{B} + \frac{\eta}{\mu_0} \nabla \times \mathbf{B}, \quad (29)$$

$$\nabla^2 \Phi = -\nabla \cdot \left[ -\mathbf{V} \times \mathbf{B} + \frac{\eta}{\mu_0} \nabla \times \mathbf{B} \right], \quad (30)$$

$$\mathbf{V} \cdot \mathbf{B} = 0. \quad (31)$$

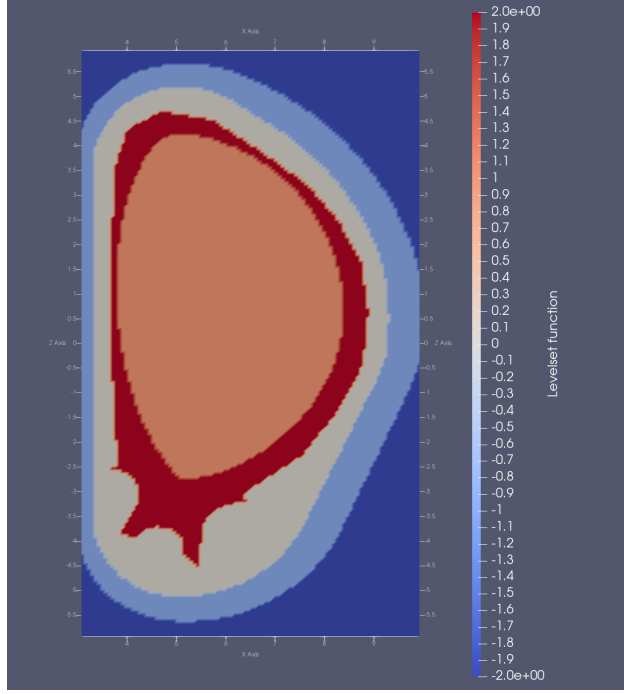


Figure 1: ITER tokamak sub-domains in the poloidal plane. The level-set function shown in the color-map indicates different physical domains: 1 in the inner area of the plasma chamber, 2 between the separatrix and the wall, 0 at the rigid wall, -1 at the vacuum vessel and -2 outside the vacuum vessel. The above configuration is used in the simulations of the numerical section.

## 2.2. Coupling to ITER blankets and vacuum vessel

The plasma in the ITER tokamak reactor is enclosed by a chamber wall, behind which are blanket modules secured on a stainless steel vacuum vessel. See Figure 1 for the ITER's poloidal cross section. The vacuum vessel (in light blue) is continuous toroidally and poloidally, so it is a good flux conserver with a wall time of about 500 ms. The blanket modules (in ivory white) are attached to the vacuum vessel, and they are constructed and arranged in such a way that a net toroidal current is impeded. To a reasonable approximation, we will approximate the entire vacuum vessel as toroidally symmetric conductor with a constant resistivity, so that the wall time is 500 ms. This simplification ignores the neutron shielding materials embedded in the vacuum vessel. The electromagnetic field is evolved inside the vacuum vessel with the standard Ohm's law of constant resistivity,

$$\frac{\partial \mathbf{B}}{\partial t} = -\nabla \times \mathbf{E}, \quad (32)$$

$$\mathbf{E} = \eta_{\text{VV}} \mathbf{j} = \frac{\eta_{\text{VV}}}{\mu_0} \nabla \times \mathbf{B}. \quad (33)$$

Since the wall time depends on inductance as well, so we numerically compute the current decay time in the vacuum vessel and match the 500 ms wall time to an effective resistivity  $\eta_{\text{VV}}$  for ITER's vacuum vessel.

For the first wall and blanket module section, we will deploy an anisotropic resistivity that has



the toroidal resistivity  $\eta_t$  much greater than the poloidal resistivity  $\eta_p$ , so

$$\frac{\partial \mathbf{B}}{\partial t} = -\nabla \times \mathbf{E}, \quad (34)$$

$$\mathbf{E} = \frac{\eta_t}{\mu_0} (\nabla \times \mathbf{B})_\phi + \frac{\eta_p}{\mu_0} \left[ \nabla \times \mathbf{B} - (\nabla \times \mathbf{B})_\phi \right] \quad (35)$$

with  $(\cdot)_\phi$  denoting the toroidal component. The ratio of  $\eta_t$  and  $\eta_p$  is chosen so that the toroidal current in the blanket is suppressed and the halo current can flow poloidally in the blankets to enter the vacuum vessel, where the electrical current can have a strong toroidal component.

### 2.3. Quasi-static perpendicular plasma dynamics model and its interface conditions

For tokamak simulations, we consider the cylindrical coordinate of  $(R, \phi, Z)$  for a direct mapping from the Cartesian coordinate  $(x, y, z)$ . The structured staggered mesh under the cylindrical coordinate is used in the current work. The tokamak computational domain is  $\Omega = [R_{\min}, R_{\max}] \times [0, 2\pi] \times [Z_{\min}, Z_{\max}]$ , which can be decomposed into two sub-domains:

$$\Omega := \Omega^P \cup \Omega^W,$$

where  $\Omega^P$  corresponds to the tokamak's plasma chamber whereas  $\Omega^W$  includes the rigid wall region, the vacuum vessel and the area outside it (see Figure 1 for details:  $\Omega^P$  comprises the areas where the level-set function is positive,  $\Omega^W$  corresponds to non-positive values of the level-set function). We use  $\Gamma^{PW}$  to denote the interface between the two subdomains  $\Omega^P$  and  $\Omega^W$ . Note that in  $\Omega^W$ , there is no plasma and thus the plasma density ( $n$ ) and velocity equations become

$$\begin{aligned} \frac{\partial n}{\partial t} &= 0 & \text{in } \Omega^W, \\ \mathbf{V}_\perp &= \mathbf{0} & \text{in } \Omega^W, \end{aligned}$$

while the fields satisfy the diffusion equation as discussed in Section 2.2.

In the sequel, we consider the model introduced in Section 2.1 for the plasma region  $\Omega^P$  with some slight adjustments:

- When compared to the perpendicular component, the parallel velocity component can be considered as negligible. Therefore, it is neglected in the density equation and not solved in the velocity equation.
- For stabilization purposes, a viscosity term is added to the velocity equations in  $R$  and  $Z$  directions (see Appendix A, Appendix B and Appendix D for some discussions on its impact).
- The resistivity is assumed to be a constant in each sub-domain.

An interface condition is needed for such a multi-domain interface problem. For the fields, the following jump conditions should be naturally satisfied,

$$[\mathbf{B} \cdot \mathbf{n}] = 0 \quad \text{on } \Gamma^{PW}, \quad (36)$$

$$[\mathbf{E} \times \mathbf{n}] = \mathbf{0} \quad \text{on } \Gamma^{PW}, \quad (37)$$

$$\mathbf{V}_{i\perp} = \mathbf{0} \quad \text{on } \Gamma^{PW}, \quad (38)$$

where  $[\cdot]$  stands for the jump operator along the interface. These conditions are consistent with the absence of surface charge/current and the fact that there is no jump in the electrical field.

Finally, the multi-domain quasi-static plasma model along with its interface condition that is considered in the current work is summarized as follows:

- In the plasma region:

$$\frac{\partial n}{\partial t} + \nabla \cdot (n \mathbf{V}_\perp) = 0 \quad \text{in } \Omega^P, \quad (39)$$

$$-\left( \nu n_0 m_i \nabla^2 \mathbf{V}_{i\perp} + \frac{1}{\mu_0} (\nabla \times \mathbf{B}) \times \mathbf{B} \right) \cdot \mathbf{e}_R = 0 \quad \text{in } \Omega^P, \quad (40)$$

$$\mathbf{V}_\perp \cdot \mathbf{B} = 0 \quad \text{in } \Omega^P, \quad (41)$$

$$-\left( \nu n_0 m_i \nabla^2 \mathbf{V}_{i\perp} + \frac{1}{\mu_0} (\nabla \times \mathbf{B}) \times \mathbf{B} \right) \cdot \mathbf{e}_Z = 0 \quad \text{in } \Omega^P, \quad (42)$$

$$-\nabla^2 \Phi - \nabla \cdot \left[ -\mathbf{V}_\perp \times \mathbf{B} + \frac{\eta}{\mu_0} (\nabla \times \mathbf{B}) \right] = 0 \quad \text{in } \Omega^P, \quad (43)$$

$$\boldsymbol{\tau} - \nabla \Phi + \mathbf{V}_\perp \times \mathbf{B} - \frac{\eta}{\mu_0} (\nabla \times \mathbf{B}) = \mathbf{0} \quad \text{in } \Omega^P, \quad (44)$$

$$\frac{\partial \mathbf{B}}{\partial t} + \nabla \times \boldsymbol{\tau} = \mathbf{0} \quad \text{in } \Omega^P. \quad (45)$$

- In the wall region:

$$\frac{\partial n}{\partial t} = 0 \quad \text{in } \Omega^W, \quad (46)$$

$$\mathbf{V}_\perp = \mathbf{0} \quad \text{in } \Omega^W, \quad (47)$$

$$-\nabla^2 \Phi - \nabla \cdot \left[ \frac{\eta}{\mu_0} (\nabla \times \mathbf{B}) \right] = 0 \quad \text{in } \Omega^W \quad (48)$$

$$\boldsymbol{\tau} - \nabla \Phi - \frac{\eta}{\mu_0} (\nabla \times \mathbf{B}) = \mathbf{0} \quad \text{in } \Omega^W, \quad (49)$$

$$\frac{\partial \mathbf{B}}{\partial t} + \nabla \times \boldsymbol{\tau} = \mathbf{0} \quad \text{in } \Omega^W. \quad (50)$$

- At the wall/plasma interface:

$$\mathbf{V}_\perp = 0 \quad \text{on } \Gamma^{PW}, \quad (51)$$

$$\boldsymbol{\tau} \times \mathbf{n} \quad \text{continuous across } \Gamma^{PW}, \quad (52)$$

$$\mathbf{B} \cdot \mathbf{n} \quad \text{continuous across } \Gamma^{PW}. \quad (53)$$

- At the outer rectangular boundary  $\partial\Omega$ :

$$\Phi = 0, \quad (54)$$

$$\boldsymbol{\tau} \times \mathbf{n} = \mathbf{0}. \quad (55)$$

Note that Equations (39) and (46) express the plasma density continuity equation and that the field of  $\boldsymbol{\tau}$  and  $\Phi$  are considered instead of the electric field due to the reason described in Section 2.1.

### 3. Mimetic finite difference discretization

This section focuses on the MFD formulation and the full multi-domain quasi-static plasma model. We consider a structured orthogonal mesh in 3D with hexahedral cells  $c$  that form a subdivision of the computation domain. Let  $|c|$ ,  $|f|$  and  $|e|$  be the volume of cell  $c$ , the area of face

$f$  and the length of edges  $e$ , respectively. We use  $\mathcal{N}_h$ ,  $\mathcal{E}_h$ ,  $\mathcal{F}_h$  and  $\mathcal{C}_h$  to denote the discrete node, edge, face and cell spaces, respectively. The MFD employed here is a staggered mesh method; the velocity and electrostatic potential unknowns are defined at mesh vertices ( $\mathbf{V}_h, \Phi_h \in \mathcal{N}_h$ ), the electric field unknowns are defined on mesh edges ( $\boldsymbol{\tau}_h \in \mathcal{E}_h$ ), the magnetic field unknowns are defined on mesh faces ( $\mathbf{B}_h \in \mathcal{F}_h$ ) while the ion number density unknowns are defined on mesh elements ( $n_{ih} \in \mathcal{C}_h$ ). We first introduce the primary and dual mimetic operators acting between the discrete spaces:

$$\begin{array}{ccccccc} \mathcal{N}_h & \longrightarrow & \mathcal{E}_h & \longrightarrow & \mathcal{F}_h & \longrightarrow & \mathcal{C}_h \\ & & \text{Grad}_h & & \text{Curl}_h & & \text{Div}_h \\ \\ \mathcal{N}_h & \xleftarrow{\quad} & \mathcal{E}_h & \xleftarrow{\quad} & \mathcal{F}_h & \xleftarrow{\quad} & \mathcal{C}_h \\ & & \text{Div}_h & & \text{Curl}_h & & \text{Grad}_h \end{array}$$

and then use them to discretize the quasi-static perpendicular plasma dynamics model.

### 3.1. Primary and derived mimetic operators

The MFD framework approximates first-order operators using coordinate-invariant formulas. We write the Stokes theorem for a finite-size mesh object, either cell  $c$  or face  $f$  or edge  $e$ . For instance,

$$\frac{1}{|c|} \int_c \nabla \cdot \mathbf{B} \, dV = \frac{1}{|c|} \oint_{\partial c} \mathbf{B} \cdot \mathbf{n} \, dS,$$

where  $\mathbf{n}$  is the unit normal vector to the surface  $\partial c$ . This gives us the following definition of the primary mimetic divergence operator

$$\text{Div}_h \mathbf{B}_h := \frac{1}{|c|} \sum_{f \in \partial c} \alpha_{c,f} |f| B_f, \quad \text{where } B_f := \frac{1}{|f|} \int_f \mathbf{B} \cdot \mathbf{n} \, dS.$$

Here  $|c|$  is the cell volume that has different formula in different coordinate systems. Similarly,  $|f|$  is the face area.  $\alpha_{c,f}$  is the orientation factor,  $\pm 1$ .

The discrete gradient and curl operators are defined in a similar fashion:

$$\text{Grad}_h v_h := \frac{1}{|e|} \int_e \nabla v \, dL = \frac{1}{|e|} (v_2 - v_1),$$

where vertices  $v_1$  and  $v_2$  are the endpoints of  $e$  and

$$\text{Curl}_h \mathbf{E}_h := \frac{1}{|f|} \int_f \nabla \times \mathbf{E} \, dS = \frac{1}{|f|} \sum_{e \in \partial f} \alpha_{f,e} |e| E_e, \quad \text{with } E_e := \frac{1}{|e|} \int_e \mathbf{E} \cdot \boldsymbol{\tau} \, dL,$$

where  $\boldsymbol{\tau}$  is the unit vector tangent to an edge  $e$  and  $\alpha_{f,e}$  is the orientation factor,  $\pm 1$ . The three primary mimetic operators satisfy the following discrete identities:

$$\text{Div}_h \text{Curl}_h = 0 \quad \text{and} \quad \text{Curl}_h \text{Grad}_h = 0. \tag{56}$$

A set of dual operators can be defined by discrete analogs of integration by parts. The dual operators preserve the duality property by design. To simplify the presentation, we consider the Green's formulas in functional spaces where the boundary integrals are zeros. An dual (injective) operator  $\widetilde{\text{Div}}_h : \mathcal{E}_h \rightarrow \mathcal{N}_h$  is (uniquely) defined via the discrete duality relationship:

$$[\text{Grad}_h p_h, \mathbf{v}_h]_{\mathcal{E}_h} = -[p_h, \widetilde{\text{Div}}_h \mathbf{v}_h]_{\mathcal{N}_h},$$

where the brackets denote inner products in the aforementioned discrete spaces. The other dual operators  $\widetilde{\text{Grad}}_h : \mathcal{C}_h \rightarrow \mathcal{F}_h$  and  $\widetilde{\text{Curl}}_h : \mathcal{F}_h \rightarrow \mathcal{E}_h$  are defined similarly:

$$\begin{aligned} [\text{Div}_h \mathbf{u}_h, p_h]_{\mathcal{C}_h} &= -[\mathbf{u}_h, \widetilde{\text{Grad}}_h p_h]_{\mathcal{F}_h}, \\ [\text{Curl}_h \mathbf{u}_h, \mathbf{v}_h]_{\mathcal{F}_h} &= [\mathbf{u}_h, \widetilde{\text{Curl}}_h \mathbf{v}_h]_{\mathcal{E}_h}. \end{aligned}$$

The dual operators also satisfy discrete identities:

$$\widetilde{\text{Div}}_h \widetilde{\text{Curl}}_h = 0 \quad \text{and} \quad \widetilde{\text{Curl}}_h \widetilde{\text{Grad}}_h = 0.$$

### 3.2. MFD discretization of the quasi-static perpendicular plasma dynamics model

To discretize the model above, we first need to define some projections and reconstructions between the spaces  $\mathcal{N}_h$ ,  $\mathcal{E}_h$ ,  $\mathcal{F}_h$  and  $\mathcal{C}_h$ . For vectors that are discrete representations of continuous functions, integer indices, e.g.,  $(i, j, k)$ , in the three directions correspond to values associated with vertices; integer indices in two directions, e.g.  $(i, j + \frac{1}{2}, k)$  correspond to values associated with edges; integer indices in one direction, e.g.  $(i + \frac{1}{2}, j, k + \frac{1}{2})$  correspond to values associated with faces; whereas non-integer indices in all directions, e.g.  $(i + \frac{1}{2}, j + \frac{1}{2}, k + \frac{1}{2})$  correspond to values associated with cells.

For any vertex-based vector  $\mathbf{W}$ , face-based vector  $\mathbf{X}$ , cell-based vector  $\mathbf{Y}$  and edge-based vector  $\mathbf{Z}$ , we define the cell-to-face projection  $\mathcal{P}_{c \rightarrow f}$  by:

$$\mathcal{P}_{c \rightarrow f}(\mathbf{Y})_{i+\frac{1}{2}, j+\frac{1}{2}, k} = \frac{1}{2} \left( (\mathbf{Y}_{i+\frac{1}{2}, j+\frac{1}{2}, k+\frac{1}{2}} + \mathbf{Y}_{i+\frac{1}{2}, j+\frac{1}{2}, k-\frac{1}{2}}) \cdot \mathbf{e}_Z \right) \mathbf{e}_Z, \quad (57)$$

$$\mathcal{P}_{c \rightarrow f}(\mathbf{Y})_{i+\frac{1}{2}, j, k+\frac{1}{2}} = \frac{1}{2} \left( (\mathbf{Y}_{i+\frac{1}{2}, j+\frac{1}{2}, k+\frac{1}{2}} + \mathbf{Y}_{i+\frac{1}{2}, j-\frac{1}{2}, k+\frac{1}{2}}) \cdot \mathbf{e}_\phi \right) \mathbf{e}_\phi, \quad (58)$$

$$\mathcal{P}_{c \rightarrow f}(\mathbf{Y})_{i, j+\frac{1}{2}, k+\frac{1}{2}} = \frac{1}{2} \left( (\mathbf{Y}_{i+\frac{1}{2}, j+\frac{1}{2}, k+\frac{1}{2}} + \mathbf{Y}_{i-\frac{1}{2}, j+\frac{1}{2}, k+\frac{1}{2}}) \cdot \mathbf{e}_R \right) \mathbf{e}_R, \quad (59)$$

the edge-to-vertex projection  $\mathcal{P}_{e \rightarrow v}$  by:

$$\begin{aligned} \mathcal{P}_{e \rightarrow v}(\mathbf{Z})_{i, j, k} &= \frac{1}{2} \left( (\mathbf{Z}_{i+\frac{1}{2}, j, k} + \mathbf{Z}_{i-\frac{1}{2}, j, k}) \cdot \mathbf{e}_R \right) \mathbf{e}_R + \frac{1}{2} \left( (\mathbf{Z}_{i, j-\frac{1}{2}, k} + \mathbf{Z}_{i, j+\frac{1}{2}, k}) \cdot \mathbf{e}_\phi \right) \mathbf{e}_\phi \\ &\quad + \frac{1}{2} \left( (\mathbf{Z}_{i, j, k-\frac{1}{2}} + \mathbf{Z}_{i, j, k+\frac{1}{2}}) \cdot \mathbf{e}_Z \right) \mathbf{e}_Z, \end{aligned} \quad (60)$$

the face-to-vertex projection  $\mathcal{P}_{f \rightarrow v}$  by:

$$\begin{aligned} \mathcal{P}_{f \rightarrow v}(\mathbf{X})_{i, j, k} &= \frac{1}{4} \left( (\mathbf{X}_{i, j+\frac{1}{2}, k+\frac{1}{2}} + \mathbf{X}_{i, j-\frac{1}{2}, k+\frac{1}{2}} + \mathbf{X}_{i, j+\frac{1}{2}, k-\frac{1}{2}} + \mathbf{X}_{i, j-\frac{1}{2}, k-\frac{1}{2}}) \cdot \mathbf{e}_R \right) \mathbf{e}_R \\ &\quad + \frac{1}{4} \left( (\mathbf{X}_{i-\frac{1}{2}, j, k-\frac{1}{2}} + \mathbf{X}_{i+\frac{1}{2}, j, k-\frac{1}{2}} + \mathbf{X}_{i-\frac{1}{2}, j, k+\frac{1}{2}} + \mathbf{X}_{i+\frac{1}{2}, j, k+\frac{1}{2}}) \cdot \mathbf{e}_\phi \right) \mathbf{e}_\phi \\ &\quad + \frac{1}{4} \left( (\mathbf{X}_{i-\frac{1}{2}, j-\frac{1}{2}, k} + \mathbf{X}_{i+\frac{1}{2}, j-\frac{1}{2}, k} + \mathbf{X}_{i-\frac{1}{2}, j+\frac{1}{2}, k} + \mathbf{X}_{i+\frac{1}{2}, j+\frac{1}{2}, k}) \cdot \mathbf{e}_Z \right) \mathbf{e}_Z, \end{aligned} \quad (61)$$

the vertex-to-edge reconstruction  $\mathcal{R}_{v \rightarrow e}$  by:

$$\mathcal{R}_{v \rightarrow e}(\mathbf{W})_{i+\frac{1}{2}, j, k} = \frac{1}{2} \left( \mathbf{e}_R \cdot (\mathbf{W}_{i+1, j, k} + \mathbf{W}_{i, j, k}) \right) \mathbf{e}_R, \quad (62)$$

$$\mathcal{R}_{v \rightarrow e}(\mathbf{W})_{i, j+\frac{1}{2}, k} = \frac{1}{2} \left( \mathbf{e}_\phi \cdot (\mathbf{W}_{i, j+1, k} + \mathbf{W}_{i, j, k}) \right) \mathbf{e}_\phi, \quad (63)$$

$$\mathcal{R}_{v \rightarrow e}(\mathbf{W})_{i, j, k+\frac{1}{2}} = \frac{1}{2} \left( \mathbf{e}_Z \cdot (\mathbf{W}_{i, j, k+1} + \mathbf{W}_{i, j, k}) \right) \mathbf{e}_Z, \quad (64)$$

the vertex-to-face reconstruction  $\mathcal{R}_{v \rightarrow f}$  by:

$$\mathcal{R}_{v \rightarrow f}(\mathbf{W})_{i+\frac{1}{2},j+\frac{1}{2},k} = \frac{1}{4} \left( \mathbf{e}_Z \cdot (\mathbf{W}_{i,j,k} + \mathbf{W}_{i,j+1,k} + \mathbf{W}_{i+1,j,k} + \mathbf{W}_{i+1,j+1,k}) \right) \mathbf{e}_Z, \quad (65)$$

$$\mathcal{R}_{v \rightarrow f}(\mathbf{W})_{i+\frac{1}{2},j,k+\frac{1}{2}} = \frac{1}{4} \left( \mathbf{e}_\phi \cdot (\mathbf{W}_{i,j,k} + \mathbf{W}_{i,j,k+1} + \mathbf{W}_{i+1,j,k} + \mathbf{W}_{i+1,j,k+1}) \right) \mathbf{e}_\phi, \quad (66)$$

$$\mathcal{R}_{v \rightarrow f}(\mathbf{W})_{i,j+\frac{1}{2},k+\frac{1}{2}} = \frac{1}{4} \left( \mathbf{e}_R \cdot (\mathbf{W}_{i,j,k} + \mathbf{W}_{i,j+1,k} + \mathbf{W}_{i,j,k+1} + \mathbf{W}_{i,j+1,k+1}) \right) \mathbf{e}_R. \quad (67)$$

Note that all these projection and reconstruction operators are second order accurate for the uniform orthogonal mesh considered.

**Remark 1.** *These projection and reconstruction operators could be generalized for non-uniform meshes.*

We use these projection and reconstruction operators as well as the mimetic operators to discretize the quasi-static model:

- In the plasma region:

$$\frac{\partial n_{i,h}}{\partial t} + \text{Div}_h(\mathcal{P}_{c \rightarrow f}(n_{i,h}) \mathcal{R}_{v \rightarrow f}(\mathbf{V}_{i\perp})) = 0 \quad \text{in } \Omega^P, \quad (68)$$

$$\begin{aligned} -\nu n_0 m_i \left( \widetilde{\text{Div}}_h(\text{Grad}_h \mathbf{V}_{i\perp,R}) - \frac{1}{R^2} \mathbf{V}_{i\perp,R} - \frac{2}{R} \mathcal{P}_{e \rightarrow v}(\text{Grad}_h \mathbf{V}_{i\perp,\phi}) \cdot \mathbf{e}_\phi \right) \\ - \left( \mathcal{P}_{e \rightarrow v}(\widetilde{\text{Curl}}_h \mathbf{B}_h) \times \mathcal{P}_{f \rightarrow v}(\mathbf{B}_h) \right) \cdot \mathbf{e}_R = 0 \quad \text{in } \Omega^P, \quad (69) \end{aligned}$$

$$\mathbf{V}_{i\perp} \cdot \mathcal{P}_{f \rightarrow v}(\mathbf{B}_h) = 0 \quad \text{in } \Omega^P, \quad (70)$$

$$-\nu n_0 m_i \left( \widetilde{\text{Div}}_h(\text{Grad}_h \mathbf{V}_{i\perp,Z}) \right) - \left( \mathcal{P}_{e \rightarrow v}(\widetilde{\text{Curl}}_h \mathbf{B}_h) \times \mathcal{P}_{f \rightarrow v}(\mathbf{B}_h) \right) \cdot \mathbf{e}_Z = 0 \quad \text{in } \Omega^P, \quad (71)$$

$$-\widetilde{\text{Div}}_h(\text{Grad}_h(\Phi_h)) - \widetilde{\text{Div}}_h \left[ -\mathcal{R}_{v \rightarrow e}(\mathbf{V}_{i\perp} \times \mathcal{P}_{f \rightarrow v}(\mathbf{B}_h)) + \widetilde{\text{Curl}}_h(\mathbf{B}_h) \right] = 0 \quad \text{in } \Omega^P, \quad (72)$$

$$\boldsymbol{\tau}_h - \text{Grad}_h(\Phi_h) + \mathcal{R}_{v \rightarrow e}(\mathbf{V}_{i\perp} \times \mathcal{P}_{f \rightarrow v}(\mathbf{B}_h)) - \widetilde{\text{Curl}}_h(\mathbf{B}_h) = \mathbf{0} \quad \text{in } \Omega^P, \quad (73)$$

$$\frac{\partial \mathbf{B}_h}{\partial t} + \text{Curl}_h(\boldsymbol{\tau}_h) = \mathbf{0} \quad \text{in } \Omega^P. \quad (74)$$

- In the wall region:

$$\frac{\partial n_{i,h}}{\partial t} = 0 \quad \text{in } \Omega^W, \quad (75)$$

$$\mathbf{V}_{i\perp} = \mathbf{0} \quad \text{in } \Omega^W, \quad (76)$$

$$-\widetilde{\text{Div}}_h(\text{Grad}_h(\Phi_h)) - \widetilde{\text{Div}}_h \left[ \widetilde{\text{Curl}}_h(\mathbf{B}_h) \right] = 0 \quad \text{in } \Omega^W \quad (77)$$

$$\boldsymbol{\tau}_h - \text{Grad}_h(\Phi_h) - \widetilde{\text{Curl}}_h(\mathbf{B}_h) = \mathbf{0} \quad \text{in } \Omega^W, \quad (78)$$

$$\frac{\partial \mathbf{B}_h}{\partial t} + \text{Curl}_h(\boldsymbol{\tau}_h) = \mathbf{0} \quad \text{in } \Omega^W. \quad (79)$$

As mentioned earlier, the derived mimetic curl operator  $\widetilde{\text{Curl}}_h$  used in (72) and (73) includes the variable coefficient  $\frac{\eta}{\mu_0}$  as  $K$  in (C.5). On the other hand, the other derived mimetic curl operator  $\widetilde{\text{Curl}}_h$  used in (69) and (71) includes only the constant  $\frac{1}{\mu_0}$ . The usage of derived mimetic

operators in the discrete model above instead of the combination of projections/reconstructions and primary mimetic operators is motivated by the need to preserve important properties of the continuum problem (see [Appendix D](#) for magnetic energy dissipation), and also to simplify the Jacobian matrix by cancelling some off-diagonal blocks using discrete identities (see [Section 4](#)).

The MFD discretization of the induction equation [\(74\)](#) and [\(79\)](#) lead to the following property.

**Proposition 1.** *Given a divergence-free initial magnetic field, the magnetic field solved from the above MFD system is divergence-free, when the primary divergence operator  $\text{Div}_h$  is considered.*

To see that, we note that for a discretization such as a backward Euler of the above system, the following identity holds

$$\begin{aligned} \text{Div}_h(\mathbf{B}_h^{n+1}) &= \text{Div}_h(\mathbf{B}_h^n) - \Delta t \text{Div}_h(\text{Curl}_h(\boldsymbol{\tau}_h^{n+1})) \\ &= \text{Div}_h(\mathbf{B}_h^n). \end{aligned}$$

That being said, the divergence-free property needs to satisfy two constraints: the initial magnetic field is divergence-free and the iterative solver has to be accurate enough. In practice, however, it is not easy to prepare a set of an initial condition with the magnetic field being divergence-free. It is also not necessary to solve the nonlinear system excessively accurately just for the divergence free property. An extra corrector stage using the solved  $\boldsymbol{\tau}_h^{n+1}$  can be performed in order to avoid the impact of the iterative solver. Such a strategy is commonly used in the constrained transport approach for ideal MHD [\[39, 40, 41\]](#). We have experimented such a strategy but found its impact to the quality of the solution is very minimal.

By the mimetic theory, we have the definitions of the derived divergence and curl operators given by [Formulas \(C.1\) and \(C.3\)](#) where the mass matrices  $\mathbb{M}_n$ ,  $\mathbb{M}_e$  and  $\mathbb{M}_f$  are in the spaces of vertex-based, edge-based and face-based unknowns, respectively. We have to think about the discrete operator  $\text{Curl}_h$  (resp.  $\text{Grad}_h$  and  $\text{Div}_h$ ) as a rectangular matrix acting from the space of edge-based (resp. vertex-based and face-based) fields to the space of face-based (resp. edge-based and cell-based) fields. We will present the detailed formulas for all the pieces in the above equations.

Consider a cylindrical mesh. The typical cell  $c$  is shown in [Figure 2](#) and the radius of the cell center is denoted by  $R_c$ . The definition of the primary curl operator for the top face of cell  $c$  in

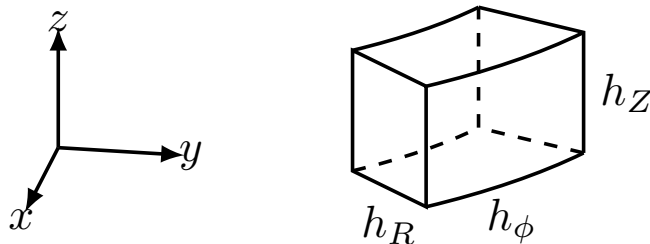


Figure 2: A typical computational cell in the configuration space used in the current work.

Figure 2 is

$$\text{Curl}_h \boldsymbol{\tau}_h = \frac{1}{|f|} \sum_{e \in \partial f} \alpha_{f,e} |e| \boldsymbol{\tau}_e = \frac{1}{|f|} \left( h_R \boldsymbol{\tau}_1 + \left( R_c + \frac{h_R}{2} \right) h_\phi \boldsymbol{\tau}_2 - h_R \boldsymbol{\tau}_3 - \left( R_c - \frac{h_R}{2} \right) h_\phi \boldsymbol{\tau}_4 \right).$$

The definition of the primary gradient operator for the number 1 edge in the top face of cell  $c$  in Figure 2 is

$$\text{Grad}_h \Phi_h = \frac{1}{|e|} \left( \Phi(R_c + \frac{h_R}{2}) - \Phi(R_c - \frac{h_R}{2}) \right) = \frac{1}{h_R} \left( \Phi(R_c + \frac{h_R}{2}) - \Phi(R_c - \frac{h_R}{2}) \right).$$

The definition of the primary divergence operator for the cell  $c$  in Figure 2 is

$$\begin{aligned} \text{Div}_h \mathbf{B}_h &= \frac{1}{|c|} \sum_{f \in \partial c} \alpha_{c,f} |f| B_f \\ &= \frac{1}{R_c h_R h_z h_\phi} (|f_{\text{right}}| B_{\text{right}} - |f_{\text{left}}| B_{\text{left}} + |f_{\text{up}}| B_{\text{up}} - |f_{\text{down}}| B_{\text{down}} + |f_{\text{front}}| B_{\text{front}} - |f_{\text{back}}| B_{\text{back}}). \end{aligned}$$

The mass matrices  $\mathbb{M}_n$ ,  $\mathbb{M}_e$  and  $\mathbb{M}_f$  are defined similarly. First, we use the additivity of integration to break the mass matrix into the sum of cell-based matrices:

$$\mathbb{M}_e = \sum_c \mathcal{N}_c \mathbb{M}_{e,c} \mathcal{N}_c^T,$$

where  $\mathcal{N}_c$  is the conventional assembly matrix. The elemental matrix  $\mathbb{M}_{e,c}$  affects the accuracy of the scheme, however, its selection does not break other mimetic properties such as the discrete exact identities. The MFD framework says that the vector-matrix-vector product should approximate the integral of underlying 3D vector functions. Recall that material properties (the coefficient  $\frac{\eta}{\mu_0}$  where the resistivity  $\eta$  may vary from a cell to another) are embedded in the derived operator  $\widetilde{\text{Curl}}_h$  via mass matrices. In this case,

$$\mathbf{u}_h^T \mathbb{M}_{e,c} \mathbf{v}_h = \frac{\mu_0}{\eta} \int_c \mathbf{u} \cdot \mathbf{v} \, dV + O(h)|c| = \frac{\mu_0}{\eta} \int_c \mathbf{u} \cdot \mathbf{v} \, r \, dr \, dz \, d\varphi + O(h)|c|.$$

By taking unitary functions  $\mathbf{u}_h$  and  $\mathbf{v}_h$  in the formula above, we could select  $\mathbb{M}_{e,c}$  to be the diagonal matrix of size 12, which is the number of edges in a cell, given by:

$$\mathbb{M}_{e,c} = \mathbb{M}_{e,c}^{(1)} := \frac{\mu_0 |c|}{\eta 4} \mathbb{I}_c. \quad (80)$$

Using the same line of thoughts, we conclude that the elemental matrix  $\mathbb{M}_{f,c}$  could be also a scalar matrix of size 6, which is the number of faces in a cell, given by:

$$\mathbb{M}_{f,c} = \frac{|c|}{2} \mathbb{I}_c. \quad (81)$$

Thus, we have for any face-based vector  $\mathbf{X}$  and edge-based vector  $\mathbf{Y}$ :

$$\mathbb{M}_f \mathbf{X} = \left[ \beta_i^f \mathbf{X}_i \right]_i; \quad \beta_i^f := \sum_{c_k \in \mathcal{C}(f_i)} \alpha_{c_k}^f; \quad \alpha_{c_k}^f := \frac{|c_k|}{2}; \quad (82)$$

$$\mathbb{M}_e^{(1)} \mathbf{Y} = \left[ \beta_l^e \mathbf{Y}_l \right]_l; \quad \beta_l^e := \sum_{c_k \in \mathcal{C}(e_l)} \alpha_{c_k}^e; \quad \alpha_{c_k}^e := \frac{\mu_0 |c_k|}{\eta(c_k) 4}; \quad (83)$$

where  $\mathcal{C}(f_l)$  denotes all cells sharing face  $f_l$  and  $\mathcal{C}(e_l)$  denotes all cells sharing edge  $e_l$ . Hence, we have all the ingredients to build the discrete derived curl operator  $\widetilde{\text{Curl}}_h$ . To form the other discrete derived curl operator  $\widehat{\text{Curl}}_h$ , it suffices to consider the following mass matrix for edge-based vectors:

$$\mathbb{M}_e^{(2)} \mathbf{Y} = \left[ \beta_l^e \mathbf{Y}_l \right]_l; \quad \beta_l^e := \sum_{c_k \in \mathcal{C}(e_l)} \underline{\alpha}_{c_k}^e; \quad \underline{\alpha}_{c_k}^e := \mu_0 \frac{|c_k|}{4}; \quad (84)$$

As for the discrete derived gradient operator  $\widetilde{\text{Div}}_h$ , the following mass matrices are needed. For any vertex-based vector  $\mathbf{W}$  and edge-based vector  $\mathbf{Y}$ :

$$\mathbb{M}_n \mathbf{W} = [\beta_j^n \mathbf{W}_j]_j; \quad \beta_j^n := \sum_{c_k \in \mathcal{C}(n_j)} \alpha_{c_k}^n; \quad \alpha_{c_k}^n := \frac{|c_k|}{8}; \quad (85)$$

$$\mathbb{M}_e^{(3)} \mathbf{Y} = [\hat{\beta}_l^e \mathbf{Y}_l]_l; \quad \hat{\beta}_l^e := \sum_{c_k \in \mathcal{C}(e_l)} \hat{\alpha}_{c_k}^e; \quad \hat{\alpha}_{c_k}^e := \frac{|c_k|}{4}. \quad (86)$$

#### 4. Solver and preconditioning strategy

This section discusses the details of the solver and block preconditioning strategy. In the most outer lever, a nonlinear solver based on Jacobian-free Newton-Krylov (JFNK) and inexact Newton is used. For the inner linear solver, a finite difference coloring Jacobian matrix is formed as a preconditioner for the Jacobian matrix inversion. Relying on the finite difference coloring approximated Jacobian turns out to be necessary in this work, since the mimetic formulations, as outlined in the previous section, involve many projections between different bases, and implementing an analytical Jacobian for such a complicated system is not practical.

The state-of-art approach for inverting such a fully coupled system is to seek an effective preconditioner. Here we outline the details of the preconditioning strategy. For ease of presentation, continuous operators are used in the following discussion. Note that the Jacobian matrix corresponding to the quasi-static perpendicular plasma dynamics model takes the form:

$$\mathbf{J} d\mathbf{U} = \begin{bmatrix} \frac{1}{dt} \mathbf{I} + (\nabla \cdot \mathbf{V}_0) \mathbf{I} + \mathbf{V}_0 \cdot \nabla & \mathbf{0} & \mathbf{0} & \mathbf{0} & n_{i,0} \nabla \cdot & +(\nabla n_{i,0}) \cdot \\ \mathbf{0} & \mathbf{I} & -\nabla & -\frac{\eta}{\mu_0} (\nabla \times \quad) + (\mathbf{V}_0 \times \quad) & -\mathbf{B}_0 \times & \\ \mathbf{0} & \mathbf{0} & -\nabla^2 & -\nabla \cdot (\frac{\eta}{\mu_0} \nabla \times \quad) + \nabla \cdot (\mathbf{V}_0 \times \quad) & -\nabla \cdot (\mathbf{B}_0 \times \quad) & \\ \mathbf{0} & \nabla \times & \mathbf{0} & \frac{1}{dt} \mathbf{I} & \mathbf{0} & \\ \mathbf{0} & \mathbf{0} & \mathbf{0} & \mathbf{C}_2 & \mathbf{C}_1 & \end{bmatrix} \begin{bmatrix} dn_i \\ d\tau \\ d\Phi \\ d\mathbf{B} \\ d\mathbf{V}_{i\perp} \end{bmatrix} \quad (87)$$

where  $\mathbf{C}_1$  and  $\mathbf{C}_2$  are different in each domain, given by:

$$\mathbf{C}_1 := \mathbf{C}_{1,p} \quad \text{in } \Omega^P, \quad (88)$$

$$\mathbf{C}_1 := \mathbf{C}_{1,w} \quad \text{in } \Omega^W, \quad (89)$$

$$\mathbf{C}_2 := \mathbf{C}_{2,p} \quad \text{in } \Omega^P, \quad (90)$$

$$\mathbf{C}_2 := \mathbf{C}_{2,w} \quad \text{in } \Omega^W; \quad (91)$$



and

$$\mathbf{C}_{1,p} = \begin{bmatrix} d\mathbf{V}_r & d\mathbf{V}_\phi & d\mathbf{V}_z \\ \frac{\nu n_0 m_i}{r^2} \mathbf{I} - \nu n_0 m_i \nabla^2 & \frac{2\nu n_0 m_i}{r^2} \frac{\partial}{\partial \phi} & \mathbf{0} \\ \mathcal{P}_{f \rightarrow v}(\mathbf{B})_{r,0} \mathbf{I} & \mathcal{P}_{f \rightarrow v}(\mathbf{B})_{\phi,0} \mathbf{I} & \mathcal{P}_{f \rightarrow v}(\mathbf{B})_{z,0} \mathbf{I} \\ \mathbf{0} & \mathbf{0} & -\nu n_0 m_i \nabla^2 \end{bmatrix} \begin{bmatrix} d\mathbf{V}_r \\ d\mathbf{V}_\phi \\ d\mathbf{V}_z \end{bmatrix}, \quad (92)$$

$$\mathbf{C}_{1,w} = \mathbf{I}, \quad (93)$$

$$\mathbf{C}_{2,p} = \quad (94)$$

$$\begin{bmatrix} d\mathbf{B}_r & d\mathbf{B}_\phi & d\mathbf{B}_z \\ -\frac{\mathbf{B}_{\phi,0}}{r} \frac{\partial}{\partial \phi} - \mathbf{B}_{z,0} \frac{\partial}{\partial z} & \left( \frac{\partial \mathbf{B}_{\phi,0}}{\partial r} - \frac{1}{r} \frac{\partial \mathbf{B}_{r,0}}{\partial \phi} + \frac{2\mathbf{B}_{\phi,0}}{r} \right) \mathbf{I} + \mathbf{B}_{\phi,0} \frac{\partial}{\partial r} & \left( \frac{\partial \mathbf{B}_{z,0}}{\partial r} - \frac{\partial \mathbf{B}_{r,0}}{\partial z} \right) \mathbf{I} + \mathbf{B}_{z,0} \frac{\partial}{\partial r} \\ \mathbf{V}_{r,0} \mathbf{I} & \mathbf{V}_{\phi,0} \mathbf{I} & \mathbf{V}_{z,0} \mathbf{I} \\ \left( \frac{\partial \mathbf{B}_{r,0}}{\partial z} - \frac{\partial \mathbf{B}_{z,0}}{\partial r} \right) \mathbf{I} + \mathbf{B}_{r,0} \frac{\partial}{\partial z} & \left( \frac{\partial \mathbf{B}_{\phi,0}}{\partial z} - \frac{1}{r} \frac{\partial \mathbf{B}_{z,0}}{\partial \phi} \right) \mathbf{I} + \mathbf{B}_{\phi,0} \frac{\partial}{\partial z} & -\frac{\mathbf{B}_{\phi,0}}{r} \frac{\partial}{\partial \phi} - \mathbf{B}_{r,0} \frac{\partial}{\partial r} \end{bmatrix} \begin{bmatrix} d\mathbf{V}_r \\ d\mathbf{V}_\phi \\ d\mathbf{V}_z \end{bmatrix}, \quad (95)$$

$$\mathbf{C}_{2,w} = \mathbf{0}. \quad (96)$$

Note that in the mimetic finite difference,  $\mathbf{C}_{2,p}$  as well as its sub-blocks are not square matrices, since  $\mathbf{V}$  and  $\mathbf{B}$  live on different positions. We indicate the corresponding locations of sub-blocks in the full Jacobian using the notations of  $d\mathbf{B}$  and  $d\mathbf{V}$ .

The linear system resulting from the linearization of the PDE is solved iteratively with a FGMRES solver preconditioned by a four-level block preconditioner that uses PETSc's fieldsplit interface. Our strategy is inspired from the recent coupled preconditioning work [63] that considered a four-field system. In the first level, the following preconditioner is used

$$\mathbf{P}^{-1} = \begin{bmatrix} \mathcal{KSP}(\mathbf{J}_{n_i}) & \mathbf{0} \\ \mathbf{0} & \mathbf{I}_{\tau\Phi\mathbf{BV}} \end{bmatrix} \begin{bmatrix} \mathbf{I}_{n_i} & -\mathbf{C}_3 \\ \mathbf{0} & \mathbf{I}_{\tau\Phi\mathbf{BV}} \end{bmatrix} \begin{bmatrix} \mathbf{I}_{n_i} & \mathbf{0} \\ \mathbf{0} & \mathcal{KSP}(\mathbf{J}_{\tau\Phi\mathbf{BV}}) \end{bmatrix}. \quad (97)$$

where  $\mathbf{C}_3$  is the top right off-diagonal block of the Jacobian matrix

$$\mathbf{C}_3 = [\mathbf{0} \quad \mathbf{0} \quad \mathbf{0} \quad n_{i,0} \nabla \cdot \quad +(\nabla n_{i,0}) \cdot], \quad (98)$$

and  $\mathcal{KSP}$  is used to denote the linear solver from PETSc. Since the bottom left block of the Jacobian matrix is zero ( $\mathbf{J}_{\tau\Phi\mathbf{BV},n_i} = \mathbf{0}$ ), such a factorization is *exact* as long as we can invert  $\mathbf{J}_{n_i}$  and  $\mathbf{J}_{\tau\Phi\mathbf{BV}}$  exactly. Note that this factorization corresponds to the ‘‘multiplicative’’ option of fieldsplit in PETSc. In particular, we use the following options for the two remaining linear solvers:

- $\mathcal{KSP}(\mathbf{J}_{n_i})$  : GMRES solver preconditioned with a block Jacobi preconditioner;
- $\mathcal{KSP}(\mathbf{J}_{\tau\Phi\mathbf{BV}})$  : FGMRES solver preconditioned with  $\mathbf{P}_{\tau\Phi\mathbf{BV}}^{-1}$ .

Now the problem is converted to looking for an efficient preconditioner  $\mathbf{P}_{\tau\Phi\mathbf{BV}}^{-1}$  for  $\mathbf{J}_{\tau\Phi\mathbf{BV}}$ , which is our second level of the block preconditioner. We use the following preconditioner based on the conventional Schur complement

$$\mathbf{P}_{\tau\Phi\mathbf{BV}}^{-1} = \begin{bmatrix} \mathbf{I}_\tau & -\mathbf{J}_{\tau,\Phi\mathbf{BV}} \\ \mathbf{0} & \mathbf{I}_{\Phi\mathbf{BV}} \end{bmatrix} \begin{bmatrix} \mathcal{KSP}(\mathbf{J}_\tau) & \mathbf{0} \\ \mathbf{0} & \mathcal{KSP}(\mathbf{S}_{\Phi\mathbf{BV}}) \end{bmatrix} \begin{bmatrix} \mathbf{I}_\tau & \mathbf{0} \\ -\mathbf{J}_{\Phi\mathbf{BV},\tau} & \mathbf{I}_{\Phi\mathbf{BV}} \end{bmatrix}. \quad (99)$$

Note that  $\mathbf{J}_\tau$  can be trivially inverted since  $\mathbf{J}_\tau$  is an identity matrix. In addition,  $\mathbf{J}_\tau$  being an identity ensures that the Schur complement  $\mathbf{S}_{\Phi\mathbf{BV}}$  can be *exactly* formed through a matrix multiplication. In particular, the Schur complement is

$$\mathbf{S}_{\{\Phi\mathbf{BV}_{i\perp}\}} d\mathbf{U} = \begin{bmatrix} -\nabla^2 & -\nabla \cdot \left(\frac{\eta}{\mu_0} \nabla \times \right) + \nabla \cdot (\mathbf{V}_0 \times \ ) & -\nabla \cdot (\mathbf{B}_0 \times \ ) \\ \mathbf{0} & \frac{1}{dt} \mathbf{I} + \nabla \times \left(\frac{\eta}{\mu_0} \nabla \times \right) - \nabla \times (\mathbf{V}_0 \times \ ) & \nabla \times (\mathbf{B}_0 \times \ ) \\ \mathbf{0} & \mathbf{C}_2 & \mathbf{C}_1 \end{bmatrix} \begin{bmatrix} d\Phi \\ d\mathbf{B} \\ d\mathbf{V}_{i\perp} \end{bmatrix}. \quad (100)$$

Note that the zero sub-block in  $\mathbf{S}_{\{\Phi\mathbf{BV}_{i\perp}\}}$  is a result of the property of the mimetic operator that guarantees the curl of the gradient operator is zero in the discrete level (up to machine precision). This shows another advantage of using the MFD discretization. Again, the overall problem is converted to finding an efficient preconditioner for  $\mathbf{S}_{\{\Phi\mathbf{BV}_{i\perp}\}}$ . In the third level, the following preconditioner is used

$$\mathbf{P}_{\Phi\mathbf{BV}}^{-1} = \begin{bmatrix} \mathcal{KSP}(\mathbf{J}_\Phi) & \mathbf{0} \\ \mathbf{0} & \mathbf{I}_{\mathbf{BV}} \end{bmatrix} \begin{bmatrix} \mathbf{I}_\Phi & -\mathbf{C}_4 \\ \mathbf{0} & \mathbf{I}_{\mathbf{BV}} \end{bmatrix} \begin{bmatrix} \mathbf{I}_\Phi & \mathbf{0} \\ \mathbf{0} & \mathcal{KSP}(\mathcal{S}) \end{bmatrix}, \quad (101)$$

where

$$\mathbf{C}_4 = \begin{bmatrix} -\nabla \cdot \left(\frac{\eta}{\mu_0} \nabla \times \right) + \nabla \cdot (\mathbf{V}_0 \times \ ) & -\nabla \cdot (\mathbf{B}_0 \times \ ) \end{bmatrix}, \quad (102)$$

and

$$\mathcal{S} = \begin{bmatrix} \frac{1}{dt} \mathbf{I} + \nabla \times \left(\frac{\eta}{\mu_0} \nabla \times \right) - \nabla \times (\mathbf{V}_0 \times \ ) & \nabla \times (\mathbf{B}_0 \times \ ) \\ \mathbf{C}_2 & \mathbf{C}_1 \end{bmatrix}. \quad (103)$$

The preconditioner  $\mathbf{P}_{\Phi\mathbf{BV}}^{-1}$  corresponds to the multiplicative option of two sub-block solvers, which is again *exact* since the bottom left block of  $\mathbf{S}_{\Phi\mathbf{BV}}$  is zero. The following options are used for the two remaining linear solvers

- $\mathcal{KSP}(\mathbf{J}_\Phi)$  : GMRES solver preconditioned with BoomerAMG preconditioner from the hypre package. Note here that  $\mathbf{J}_\Phi = -\nabla^2$ ;
- $\mathcal{KSP}(\mathcal{S})$  : A direct solver (SuperLU-DIST) is used.

The advantage of our preconditioning is that except for the sub-block solvers for  $\mathbf{J}_{n_i}$  and  $\mathbf{J}_\Phi$ , the factorization and solver strategy is *exact*. This is an outcome of the proposed preconditioning strategy and the properties of the mimetic operators. In addition, the solver for  $\mathbf{J}_\Phi$  is scalable due to algebraic multigrid being used. Overall, the nonlinear solver and the preconditioner perform very well in practice, which will be demonstrated in the numerical section.

As expected, majority of the computational time comes from the inversion of the operator  $\mathcal{S}$ . The coupling between  $\mathbf{B}$  and  $\mathbf{V}$  in  $\mathcal{S}$  is non-conventional. In particular, we find that there is a strong off-diagonal coupling in this sub-system. Note that the commonly used physics-based preconditioning strategy through parabolization [50, 48] does not work since this sub-system does not propagate the wave. We leave it to the future study for an algorithmic scalable solver. Nevertheless, the above preconditioner is sufficient for the problems considered in this work. The typical walltime to take a single time step using the proposed solver is about half a minute on 128 CPUs. In comparison, a direct solver or an iterative solver preconditioned with a generic preconditioner such as block incomplete LU need several hours to invert the same system.

## 5. Numerical results

In this section, numerical simulations are used to assess the performance of the MFD solver in solving the quasi-static force-free model (Equations (39)–(54)) with different configurations. The simulations were carried out on NERSC’s Cori and Perlmutter machines. For our computations on Cori, we used 4 Haswell nodes for a total of 128 cpus. For our computations on Perlmutter, we used 1 CPU-only node for a total of 128 cpus.

For parallelization, we employ the Parallel Extensible Toolkit for Scientific computing (PETSc) library [64, 65, 66]. For the time-integration, we rely on PETSc’s TS library that provides a framework for the scalable solvers of ODEs and DAEs arising from the discretization of time-dependent PDEs [67]. The major data structure we build our MFD algorithm upon is DMStag [68], which is PETSc’s distributed data structure for a full set of staggered grid representations. This allows the degrees of freedom to be associated with all “strata” in a logically-rectangular grid, i.e., elements, faces, edges, and vertices. Note that such representations are more than the commonly used dual mesh setting such as those in FDTD. We use a second-order L-stable DIRK time integrator and JFNK preconditioned by the finite difference coloring Jacobian. Our major criterion for the solver convergence is the relative tolerance of the Newton iteration, which is always set as  $1 \times 10^{-4}$ . The linear solver tolerance is dynamically controlled by the inexact Newton algorithm, which is used to reduce the total number of linear iterations.

All the simulations presented in the current work are run on a cylindrical mesh that has a resolution of  $100 \times 2 \times 200$ , i.e., 100 cells in  $R$  direction, 2 cells with periodic boundary conditions in  $\phi$  direction and 200 cells in  $Z$  direction. A minimal number of grid points in  $\phi$  direction are used since we only consider the axisymmetric case in this work. However, we maintain a general implementation of full 3D operators, aiming for the whole device modeling capability and study of asymmetric cases in the future work.

The numerical results are organized into five sections. Section 5.1 first investigates the impact of resistivity in the vacuum vessel. Since the model considered here misses a temperature equation (it will be considered as the immediate follow-up work), the physically relevant resistivity value can be only determined numerically. We propose a simple approach to evaluate the model using the diffusion model in the vacuum vessel. Section 5.2 then discusses the steps to prepare the initial condition. As an exactly force-free magnetic field is known to be challenging to find, we propose a modeling approach to further reduce the  $\mathbf{j} \times \mathbf{B}$  force. The impact of different regularization terms are then studied in Section 5.3. The full VDE simulation is presented in Section 5.4. Finally, the study of the solver performance is presented in Section 5.5.

### 5.1. Computing the effective resistivity of ITER vacuum vessel

The ITER tokamak reactor has an interesting engineering design in which the vacuum vessel (vv) is to carry the inductive toroidal current as the response to a dynamically evolving plasma, such as that during a VDE after a thermal quench. To enable this, the blanket modules, which are attached to the vacuum vessel and face the plasma, are insulated from each other along the toroidal direction so no net toroidal current is allowed in the blanket modules. To model the plasma VDE properly, one must properly account for the image current, especially the toroidal one, in the vacuum vessel. The actual ITER vacuum vessel has complicated structures and a hollow interior for neutron moderating inserts, the details of which are not necessary in the usual plasma modeling. The essential property of the vacuum vessel for plasma modeling is its characteristic time for a wall current to decay in the absence of a plasma inside the chamber. This so-called wall time of the vacuum vessel,  $\tau_{vv} \equiv L/R$ , is the ratio of inductance  $L$  and resistance  $R$  of the metal structure. The inductance  $L$  is set by the geometry of the conducting structure, while  $R$  has separate toroidal

and poloidal values, corresponding to the decay of a net toroidal and a poloidal current in the vacuum vessel. For wall feedback on VDEs, the toroidal one is most important, and for ITER, the toroidal wall time is known to be around 500 ms. The geometric simplification of the vacuum vessel, shown in light blue (value of -1 for the levelset function) in Figure 1, implies that the correct  $\tau_{\text{VV}} = 500$  ms can be recovered by an effective electric resistivity  $\eta_{\text{VV}}$  for the vacuum vessel that would be somewhat different from  $\eta$  of the stainless steel that is used to construct the vacuum vessel. This effective  $\eta_{\text{VV}}$  is directly computed here to match a given  $\tau_{\text{VV}}$  as follows.

The goal here is to consider an isotropic vacuum vessel with uniform resistivity, and find the resistivity value that would yield the targeted wall time for ITER setting (around 500 ms). For that purpose, we run initial stand-alone tests for the magnetic diffusion problem where we take the same high resistivity value (to mimic a vacuum response) for all the computational domain except the vacuum vessel, and a lower resistivity value for the vacuum vessel  $\Omega^V$ . The initial magnetic field has to be set such that the current is nonzero only in the vacuum vessel. We recall that the magnetic field in the tokamak can be represented by

$$\mathbf{B} = \nabla\phi \times \nabla\psi + g_0\nabla\phi, \quad (104)$$

where  $\psi$  is the poloidal flux function and  $g_0$  is a scalar constant.

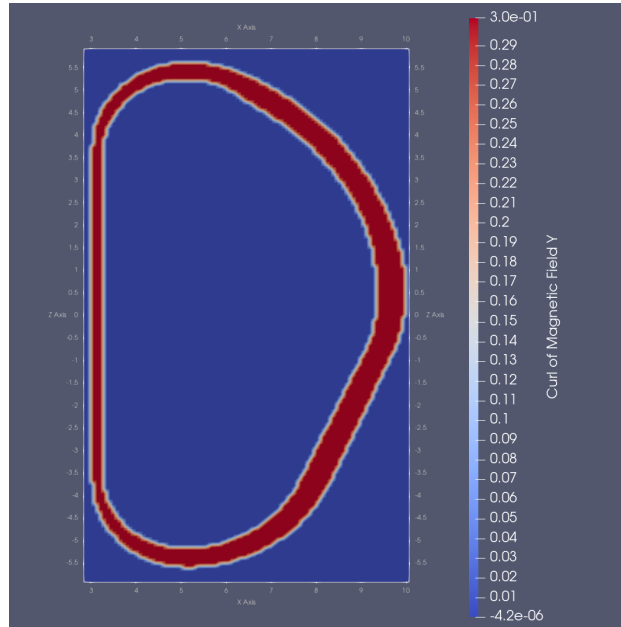


Figure 3: The curl of the initial magnetic field in  $\mathbf{e}_\phi$  direction.

Enforcing a magnetic field such that the current is nonzero only in the vacuum vessel amounts to solving the fixed-boundary Grad-Shafranov problem

$$\begin{aligned} \frac{1}{\mu_0 R} \Delta^* \psi &= J_0 & \text{in } \Omega^V, \\ \frac{1}{\mu_0 R} \Delta^* \psi &= 0 & \text{in } \Omega \setminus \Omega^V, \\ \psi &= 0, & \text{on } \partial\Omega; \end{aligned} \quad (105)$$

where the toroidal elliptic operator is defined as

$$\Delta^* \psi := \frac{\partial^2 \psi}{\partial R^2} - \frac{1}{R} \frac{\partial \psi}{\partial R} + \frac{\partial^2 \psi}{\partial Z^2},$$

After solving the problem (105), and computing the magnetic field with (104), we obtain the current shown in Figure 3.

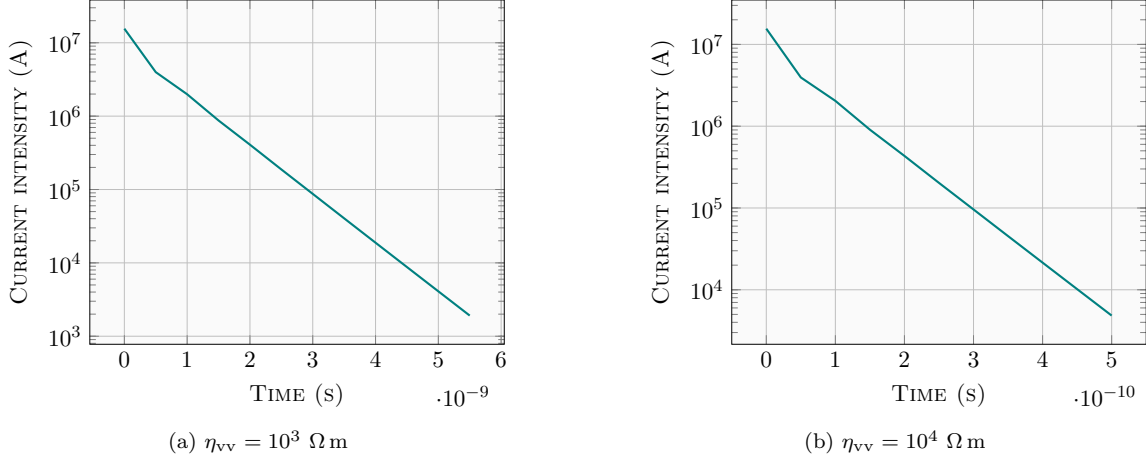


Figure 4: Evolution of the current intensity inside the vacuum vessel over time with two different vacuum vessel resistivities  $\eta_{vv}$  and a fixed resistivity elsewhere  $\eta = 10^6 \Omega \text{ m}$ .

Then, the diffusion model (Equations (46)–(50)) is solved. With a resistivity value of  $\eta_{vv} = 1 \times 10^3 \Omega \text{ m}$  (i.e., a Lundquist number  $S_{vv} = 2.7646 \times 10^{-2}$  if the resistive diffusion time is normalized by the plasma Alfvén time) inside the vacuum vessel and  $\eta = 1 \times 10^6 \Omega \text{ m}$  ( $S = 2.7646 \times 10^{-5}$ ) elsewhere, we obtain the current evolution depicted in Figure 4a. The slope is estimated as

$$a_1 := \frac{\ln(10^5) - \ln(10^6)}{3 \times 10^{-9} - 1.5 \times 10^{-9}} = -1.53 \times 10^9 \text{ s}^{-1}.$$

With a resistivity value of  $\eta_{vv} = 1 \times 10^4 \Omega \text{ m}$  (i.e., a Lundquist number  $S_{vv} = 2.7646 \times 10^{-3}$ ) inside the vacuum vessel and  $\eta = 1 \times 10^6 \Omega \text{ m}$  ( $S = 2.7646 \times 10^{-5}$ ) elsewhere, we obtain the current evolution depicted in Figure 4b. The slope is now equal to:

$$a_2 := \frac{\ln(10^5) - \ln(10^6)}{3 \times 10^{-10} - 1.5 \times 10^{-10}} = -1.53 \times 10^{10} \text{ s}^{-1}.$$

The characteristic time scale  $L/R$  or wall time is expressed as

$$\tau_{vv} = \frac{L}{R_t},$$

with  $L$  the inductance and the toroidal resistance

$$R_t = \frac{2\pi R \eta}{\mathcal{A}};$$

$\mathcal{A}$  being the cross section. The current decay is such that

$$I(t) = I_0 \exp\left(-\frac{t}{\tau_{vv}}\right).$$

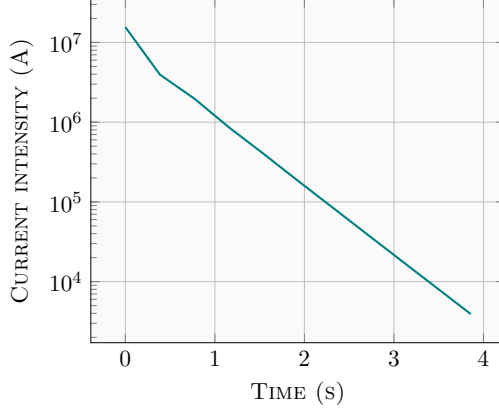


Figure 5: Evolution of the current intensity inside the vacuum vessel over time with  $\eta_{\text{vv}} = 1.30288 \times 10^{-6} \Omega \text{ m}$ .

With the slopes computed previously, we can deduce that the resistivity value corresponding to  $\tau_{\text{vv}} = 500 \text{ ms}$  is:

$$\eta_{\text{vv}} = 1.30288 \times 10^{-6} \Omega \text{ m}. \quad (106)$$

With such a resistivity ( $S_{\text{vv}} = 21219200$ ) inside the vacuum vessel and  $\eta = 1.30288 \times 10^{-3} \Omega \text{ m}$  ( $S = 21219.2$ ) elsewhere, we obtain the current evolution depicted in Figure 5. The slope is equal to:

$$a_3 := \frac{\ln(3922.26) - \ln(860919)}{3.858030 - 1.157409} = -1.99633062361 \text{ s}^{-1},$$

which is very close to the expected value  $\frac{-1}{\tau_{\text{vv}}} = \frac{-1}{0.5} = -2 \text{ s}^{-1}$ .

### 5.2. Preparing the initial state for the quasi-static force-free model

This section discusses the preparation of the initial condition which will be used in all the rest numerical tests. The quasi-static force-free model targets a post-thermal-quench plasma in which the plasma beta is negligibly small. We prepare such an initial force-free state via a free-boundary Grad-Shafranov solver [69] by zeroing out the plasma beta of an original full-beta 15 MA ITER equilibrium, while holding the poloidal magnetic flux fixed from the original full-beta 15 MA free-boundary Grad-Shafranov equilibrium. This frozen flux boundary condition simply reflects the fact that on the time scale of the thermal quench, which is anticipated to be on the order of a millisecond and hence much shorter than the vacuum vessel wall time, the vacuum vessel acts like a perfect flux conserver. This initial state thus has zero pressure gradient, 15 MA of toroidal plasma current, and one x-point at the bottom. The details of the force-free equilibrium solver can be found in Ref. [69]. The numerical solution, once transferred to the staggered grid of the mimetic finite difference solver, has  $(\nabla \times \mathbf{B}) \times \mathbf{B}$  that is not exactly zero but close to  $10^{-3}$ , and that introduces an error at the first time step of the quasi-static model in Equations (40) and (42) since the initial velocity is nil. This gross violation of force-free condition creates difficulties for the quasi-static force-free solver at the Newton iteration of the first time step.

A workaround for this issue is to call a time-dependent model that would decrease  $(\nabla \times \mathbf{B}) \times \mathbf{B}$  and also compute a velocity that would restore some balance in Equations (40) and (42). This time-dependent model is as follows.

- In the plasma region:

$$m_i n_0 \frac{\partial \mathbf{V}_{i\perp}}{\partial t} - \nu m_i n_0 \nabla^2 \mathbf{V}_{i\perp} - \frac{1}{\mu_0} (\nabla \times \mathbf{B}) \times \mathbf{B} = \mathbf{0} \quad \text{in } \Omega^P, \quad (107)$$

$$-\nabla^2 \Phi + \nabla \cdot [\mathbf{V}_{i\perp} \times \mathbf{B}] = 0 \quad \text{in } \Omega^P, \quad (108)$$

$$\boldsymbol{\tau} - \nabla \Phi + \mathbf{V}_{i\perp} \times \mathbf{B} = \mathbf{0} \quad \text{in } \Omega^P, \quad (109)$$

$$\frac{\partial \mathbf{B}}{\partial t} + \nabla \times \boldsymbol{\tau} = \mathbf{0} \quad \text{in } \Omega^P. \quad (110)$$

- In the wall region:

$$\mathbf{V}_{i\perp} = \mathbf{0} \quad \text{in } \Omega^W, \quad (111)$$

$$-\nabla^2 \Phi = 0 \quad \text{in } \Omega^W \quad (112)$$

$$\boldsymbol{\tau} - \nabla \Phi = \mathbf{0} \quad \text{in } \Omega^W, \quad (113)$$

$$\frac{\partial \mathbf{B}}{\partial t} + \nabla \times \boldsymbol{\tau} = \mathbf{0} \quad \text{in } \Omega^W. \quad (114)$$

- At the wall/plasma interface:

$$\mathbf{V}_{i\perp} = 0 \quad \text{on } \Gamma^{PW}, \quad (115)$$

$$\Phi \quad \text{continuous across } \Gamma^{PW}, \quad (116)$$

$$\boldsymbol{\tau} \times \mathbf{n} \quad \text{continuous across } \Gamma^{PW}. \quad (117)$$

$$\mathbf{B} \cdot \mathbf{n} \quad \text{continuous across } \Gamma^{PW}, \quad (118)$$

- At the outer rectangular boundary  $\partial\Omega$ :

$$\mathbf{V}_{i\perp} = \mathbf{0}, \quad (119)$$

$$\Phi = 0, \quad (120)$$

$$\boldsymbol{\tau} = \mathbf{0}, \quad (121)$$

$$\mathbf{B} = \mathbf{B}_0. \quad (122)$$

Here the resistivity diffusion is deliberately turned off. Note that unlike the quasi-static model, this time-dependent model has an inertia term in (107), and thus it supports the Alfvén wave and is subject to the time step constraint due to the wave. A physics-based preconditioner for the small flow limit of a similar extended MHD model was proposed in Ref. [50]. This preconditioner is extended to our MFD solver for efficiently inverting the linearized system.

Evolving the model produces a magnetic field that has a much smaller force balancing than the original field loaded into the MFD solver. In the final step of the initial condition preparation, the resulting velocity  $\mathbf{V}_{i\perp,0}$  and magnetic field  $\mathbf{B}_0$  from this time-dependent model are then used to update  $\boldsymbol{\tau}_0$  the divergence-free component of the electric field and  $\Phi_0$  the electrostatic potential such that we have

- in the plasma region:

$$-\nabla^2 \Phi_0 - \nabla \cdot \left[ -\mathbf{V}_{i\perp,0} \times \mathbf{B}_0 + \frac{\eta}{\mu_0} (\nabla \times \mathbf{B}_0) \right] = 0 \quad \text{in } \Omega^P,$$

$$\boldsymbol{\tau}_0 - \nabla \Phi_0 + \mathbf{V}_{i\perp,0} \times \mathbf{B}_0 - \frac{\eta}{\mu_0} (\nabla \times \mathbf{B}_0) = \mathbf{0} \quad \text{in } \Omega^P,$$

- in the wall region:

$$\begin{aligned} -\nabla^2\Phi_0 - \nabla \cdot \left[ \frac{\eta}{\mu_0} (\nabla \times \mathbf{B}_0) \right] &= 0 & \text{in } \Omega^W \\ \boldsymbol{\tau}_0 - \nabla\Phi_0 - \frac{\eta}{\mu_0} (\nabla \times \mathbf{B}_0) &= \mathbf{0} & \text{in } \Omega^W, \end{aligned}$$

This last step is necessary to guarantee the initial condition is consistent with the quasi-static model. Finally, we set a uniform initial density of  $n_0 = 1 \times 10^{20} \text{ m}^{-3}$  and that completes the initial state  $(n_0, \mathbf{V}_{i\perp,0}, \Phi_0, \boldsymbol{\tau}_0, \mathbf{B}_0)$  for the quasi-static model.

### 5.3. Comparing the different regularizations

As noted in section 2.1, the quasi-static force-free model requires regularization that invokes either a fictitious drag coefficient  $\epsilon$  or an artificial viscosity  $\nu$ . Since they enter directly into the force-balance equation that would otherwise constrain the magnetic field to be force-free, we anticipate their presence will modify the quasi-static dynamics but the effect will diminish as  $\epsilon$  or  $\nu$  gets smaller. This is a convergence issue related to modeling  $\mathbf{B}(\mathbf{x}, t)$  as a function of decreasing  $\epsilon$  and  $\nu$ . It is important to note that with smaller  $\epsilon$  or  $\nu$ , the regularization becomes weaker so the numerical matrix inversion for the implicit solve of the quasi-static model becomes more difficult computationally. So a practically useful regularization scheme should produce good convergence in  $\mathbf{B}(\mathbf{x}, t)$  solution for modestly small  $\epsilon$  or  $\nu$ . For this convergence check, we will gauge the quality of the solution for  $\mathbf{B}$  through two quantities. The first is the vertical position of the magnetic axis  $Z_a$  as a function of time during a VDE. The second is the total toroidal plasma current in the chamber,  $I_p(t)$ , as a function of time during a VDE. Next we first explain the set up of the test case, and then show how  $Z_a(t)$  and  $I_p(t)$  scale with  $\epsilon$  and  $\nu$ .

We consider a 5-layer configuration for the resistivity as shown in Figure 1 with the following resistivity values:

- $\eta = 9.66 \times 10^{-6} \Omega \text{ m}$  in the plasma chamber corresponding to values 1 and 2 for the levelset function in Figure 1;
- $\eta = 4.4 \times 10^{-2} \Omega \text{ m}$  in the blanket module corresponding to a value of 0 for the levelset function in Figure 1;
- $\eta = 1.30288 \times 10^{-6} \Omega \text{ m}$  in the vacuum vessel corresponding to a value of -1 for the levelset function in Figure 1;
- $\eta = 1.30288 \times 10^{-3} \Omega \text{ m}$  in the region outside the wall corresponding to a value of -2 for the levelset function in Figure 1.

and compare the results of the quasi-static models with fictitious drag term (27) and with fictitious viscous term (24) using different viscosity and drag coefficients. We plot the evolution in time of the  $z$  coordinate of the magnetic axis and the current intensity in Figures 6 and 7. Note that after normalization of Equation (24),  $\mu_0\nu$  gets replaced by the viscosity coefficient  $1/Re$ .

We observe in Figures 6 and 7 that there is no significant change in the curves for the current intensity and magnetic axis coordinate when we vary the viscosity/drag coefficients, which could indicate that the regularized model has already converged with such values and there is no need to further decrease the regularization term as that would induce more computational effort for the solver but with little and insignificant impact on the relevant physical indicators or properties.



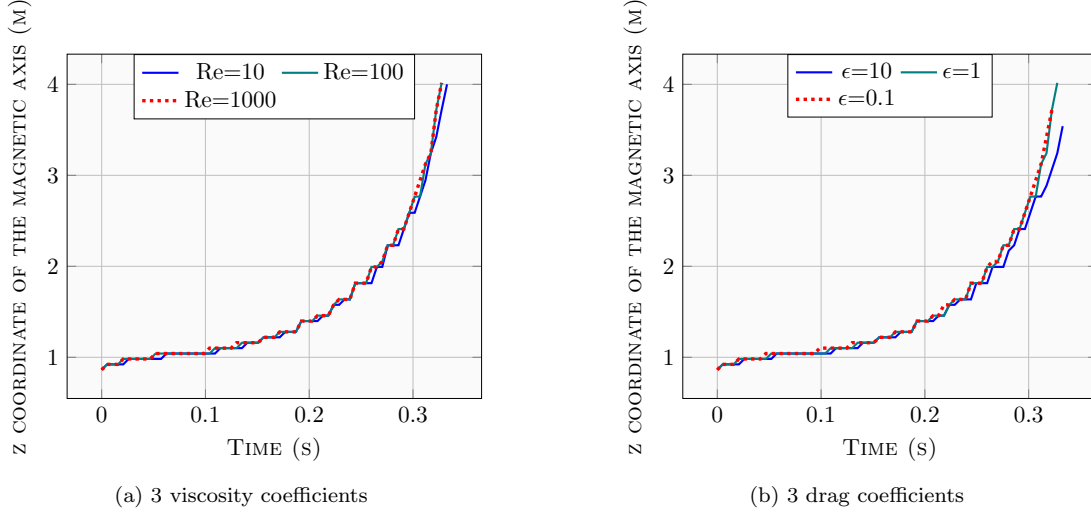


Figure 6: Evolution of the  $z$  coordinate of the magnetic axis over time for different viscosity and drag coefficients.

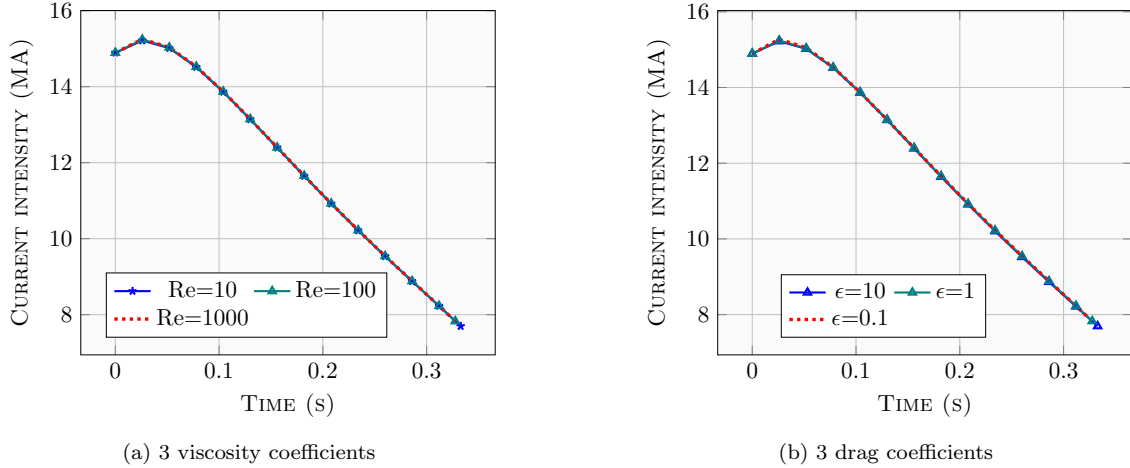


Figure 7: Evolution of the current intensity inside the plasma chamber over time with different artificial viscosity and fictitious drag coefficients.

A subtler effect of regularization, as explained in Section 2.1, is that it sets a radial electric field  $\varphi(\psi)$ , which is not constrained by the quasi-static force-free model. This is thus an artificial radial electric field, which interestingly enough, does not modify the magnetic field evolution directly, since the curl of an electrostatic field vanishes in the Faraday's law. In Fig. 8, we numerically compute  $\varphi(\psi)$  from  $\Phi(R, Z)$  by performing an average of  $\Phi$  along the field lines which are contours of poloidal magnetic flux  $\psi$ . This  $\varphi(\psi)$  is then plotted as a function of  $\psi$ . Here we shall classify two classes of magnetic field lines or constant  $\psi$  surfaces (contour lines in the poloidal cross section of an axisymmetric configuration). Where  $\psi$  forms closed contours in the plasma domain, one has closed flux surfaces. There are regions in which  $\psi$  contours or magnetic field lines intercept the chamber wall, these are known as the open flux or magnetic field line region. Since the chamber wall is a conductor and  $\Phi$  is set to zero there, so  $\varphi$  on the open flux region is close to zero, in the order of  $10^{-10}$  to  $10^{-8}$  (normalized unit) range. The radial electrostatic potential  $\varphi(\psi)$  can take on a much larger value inside the closed flux region, resulting in a sizable radial electric field across the separatrix (if it exists) or the last closed flux surface that scrapes off the chamber wall.

By comparing Fig. 8a and Fig. 8b, one can see that both the fictitious drag ( $\epsilon$ ) and artificial viscosity ( $\nu$ ) produce  $\varphi(\psi)$  of comparable amplitude. In the case of artificial viscosity, the  $Re = 100$  and  $Re = 1000$  cases appear to converge to the same  $\varphi(\psi)$ . The fictitious drag coefficients of  $\epsilon = 10$  and  $\epsilon = 0.1$  evidently yield  $\varphi(\psi)$  with sizable difference in the closed flux region. That is also the case after 25 time steps in Figure 9. It should be emphasized again that the  $\varphi(\psi)$  so produced is an artificial radial electric field, entirely the result of the regularization scheme. The quasi-static MHD model itself does not physically constrain  $\varphi(\psi)$ .

At a later time, all the fictitious drag and artificial viscosity coefficients produce almost identical  $\varphi(\psi)$  amplitudes. This could be observed in Figure 10 that shows the curves of electrostatic potential average in function of the poloidal magnetic flux function after 50 time steps, which corresponds to the time when the magnetic axis moves to mid-way (in vertical position) between the eventual impact point at the first wall and the initial state. The same observation holds after 56 time steps in Figure 11.

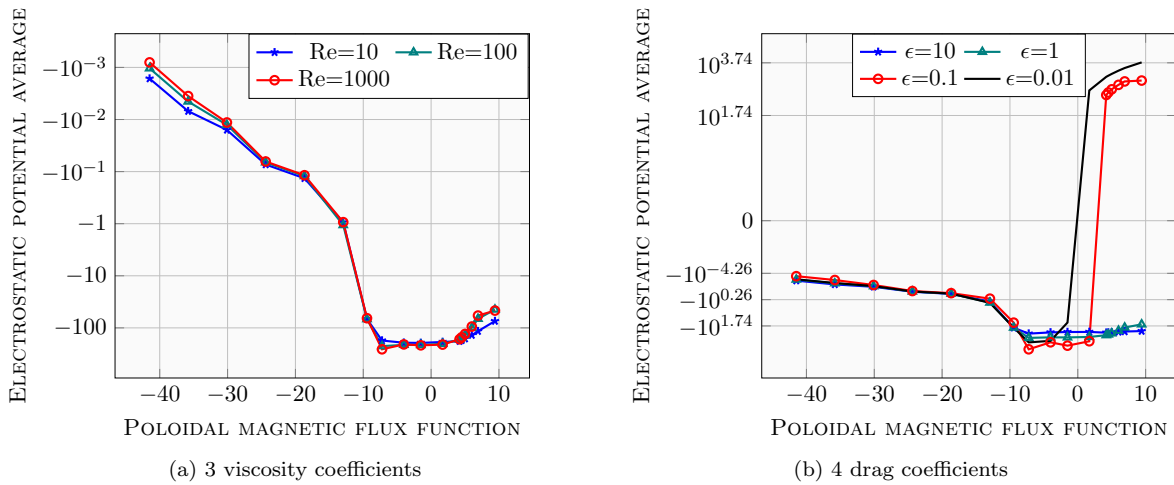


Figure 8: Evolution of the electrostatic potential average over poloidal magnetic flux function with different artificial viscosity and fictitious drag coefficients at the first time step.

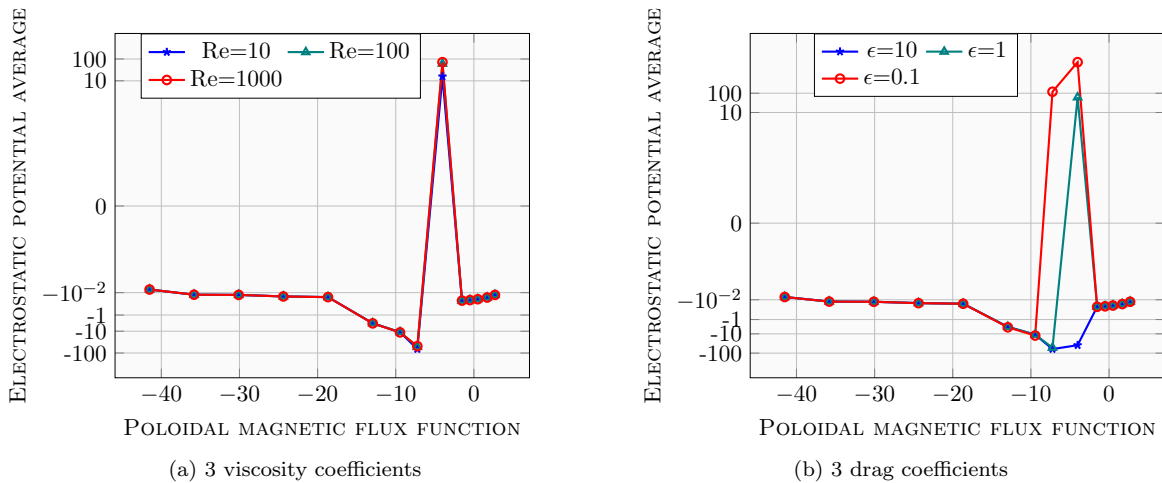


Figure 9: Evolution of the electrostatic potential average over poloidal magnetic flux function with different artificial viscosity and fictitious drag coefficients after 25 time steps.

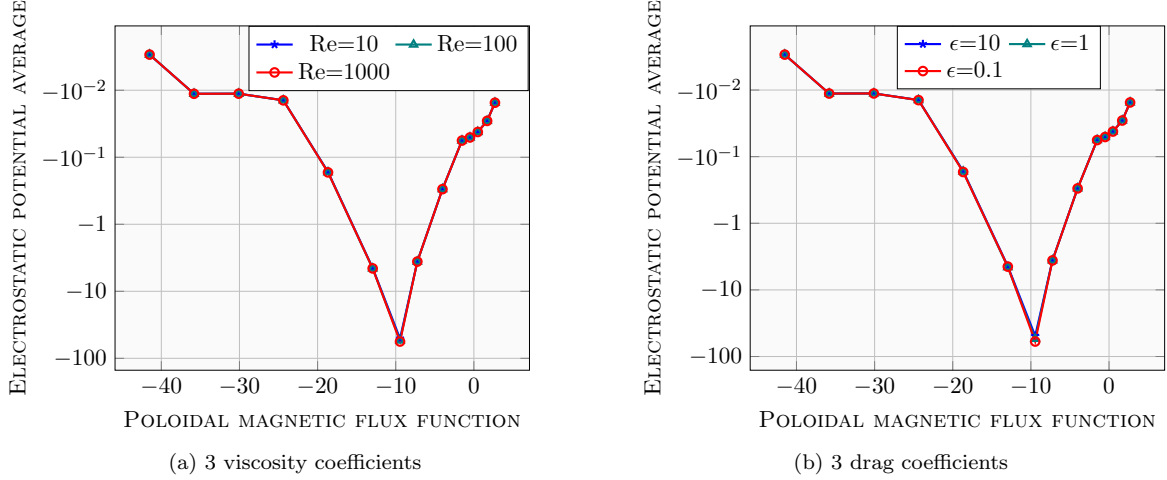


Figure 10: Evolution of the electrostatic potential average over poloidal magnetic flux function with different artificial viscosity and fictitious drag coefficients after 50 time steps.

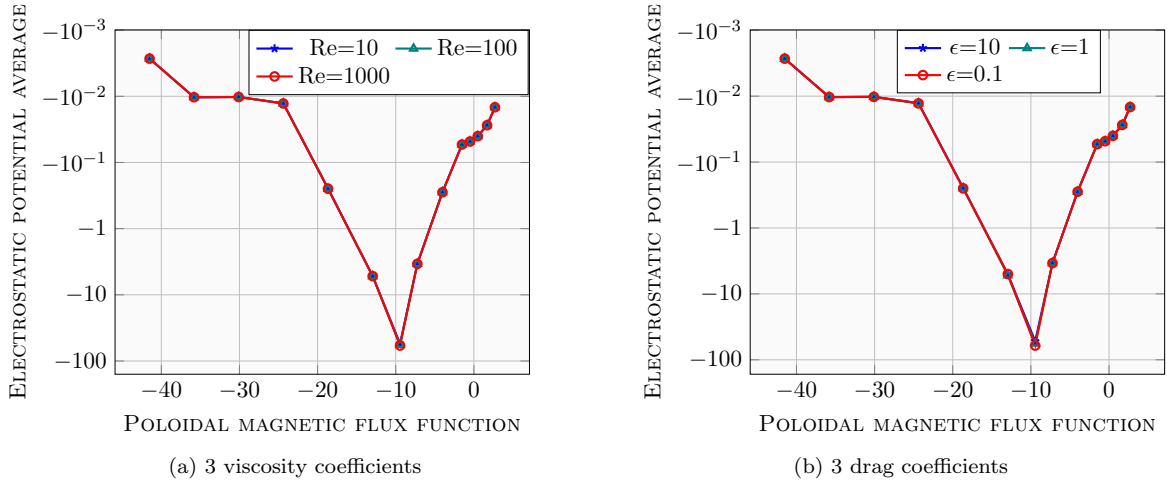


Figure 11: Evolution of the electrostatic potential average over poloidal magnetic flux function with different artificial viscosity and fictitious drag coefficients after 56 time steps.

Figures 12–14 and 15–18 show the poloidal magnetic flux function and the electrostatic potential respectively with different artificial viscosity coefficients at the first time step and after 50 time steps. The former figures show that the poloidal magnetic flux function is identical for the three viscosity coefficients whereas the latter figures show that there are differences in the electrostatic potential but these tend to be rather minimal.

#### 5.4. Full cold ITER VDE simulation

In this section, we present the results of a full ITER VDE simulation. We distinguish two settings for the blanket module: isotropic resistivity and anisotropic resistivity. In the isotropic case, a higher resistivity inhibits both toroidal and poloidal current flowing inside the blanket. The wall current mostly resides in the vacuum vessel, driven by inductively by the inductive electric field. For the anisotropic case, the poloidal resistivity is sufficiently reduced that poloidal current can flow inside the blanket but the toroidal current is still inhibited by a higher toroidal resistivity. The poloidal current in the blanket now provides the pathways for halo current that enters the blanket

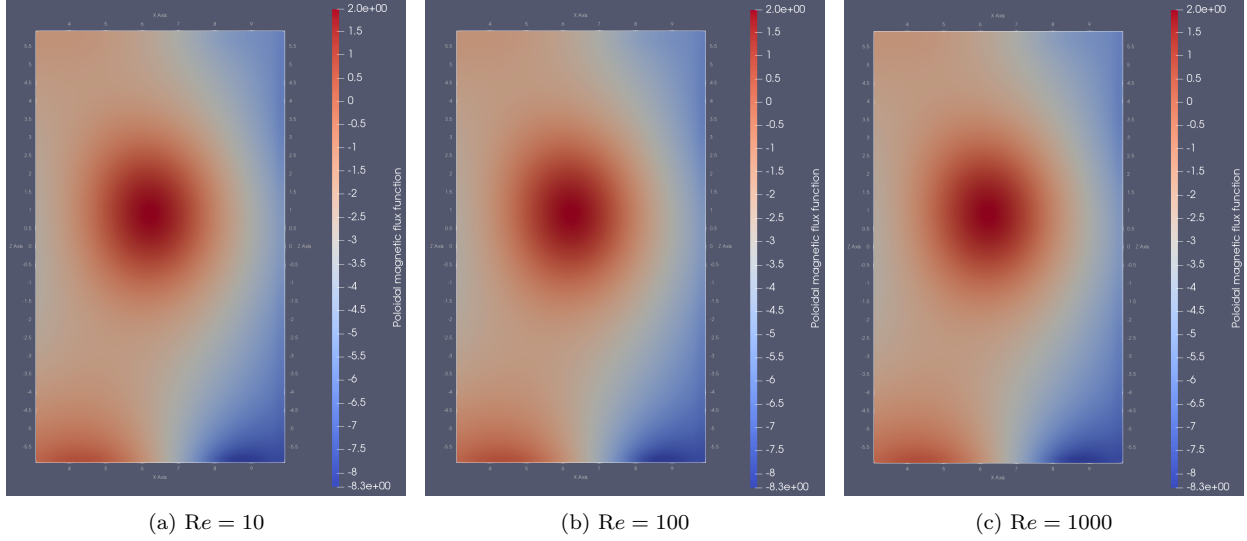


Figure 12: The poloidal magnetic flux function with different artificial viscosity coefficients at the first time step

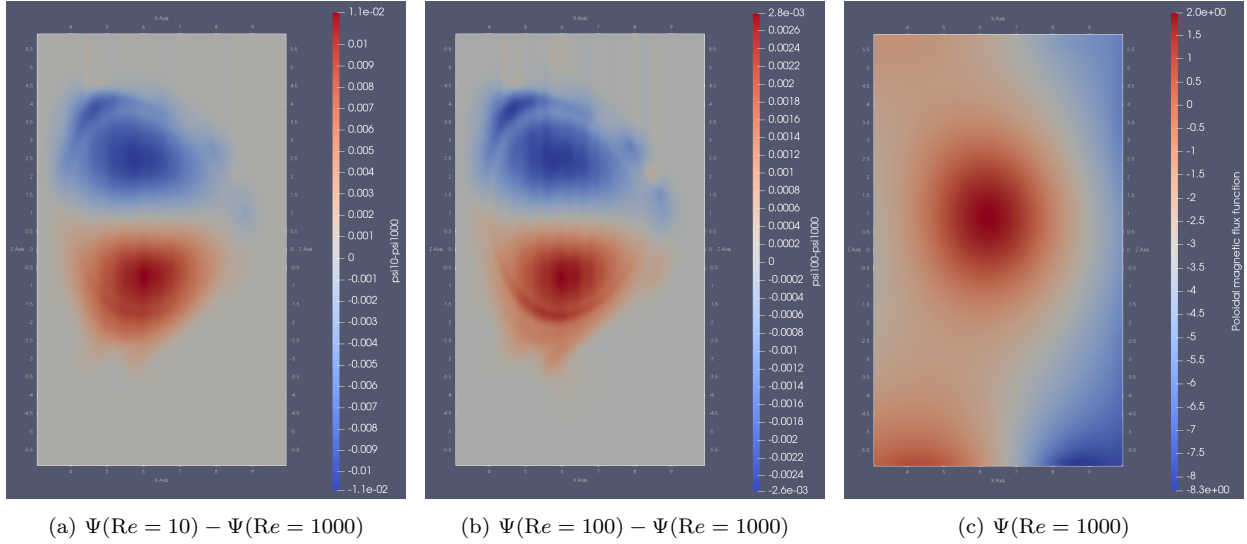


Figure 13: The poloidal magnetic flux function for  $Re = 1000$  and the differences  $\Psi(Re = 100) - \Psi(Re = 1000)$  and  $\Psi(Re = 10) - \Psi(Re = 1000)$  at the first time step.

from the plasma, poloidally tranverses the blanket, and then exit into the vacuum vessel, and vice versa.

#### 5.4.1. Isotropic setting

First, we consider the resistivity setting described in Section 2.1 and a fictitious viscosity regularization term with  $Re = 1000$ . The VDE phenomenon is illustrated in Figure 19 where we notice that vertical motion of the plasma column is correlated with the resistive dissipation of the plasma current. The toroidal current,  $j_\phi := (\nabla \times \mathbf{B})_\phi$ , in the blanket is minimal because of the much higher material resistivity there. In contrast, much toroidal current can be inductively driven in the vacuum vessel, which has a much lower resistivity that gives rise to the 500 ms wall time for the ITER vacuum vessel. The magnetic field lines are also projected to the poloidal plane in Figure 19. It is noted that simultaneously the magnetic axis (the o-point of the streamlines) progressively moves

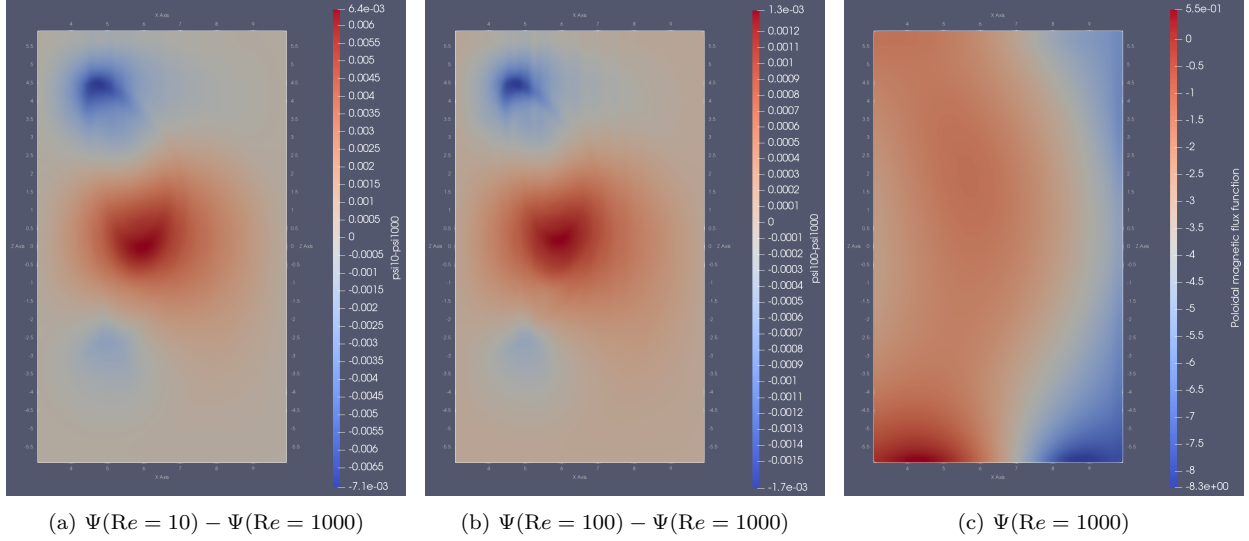


Figure 14: The poloidal magnetic flux function for  $\text{Re} = 1000$  and the differences  $\Psi(\text{Re} = 100) - \Psi(\text{Re} = 1000)$  and  $\Psi(\text{Re} = 10) - \Psi(\text{Re} = 1000)$  after 50 time steps.

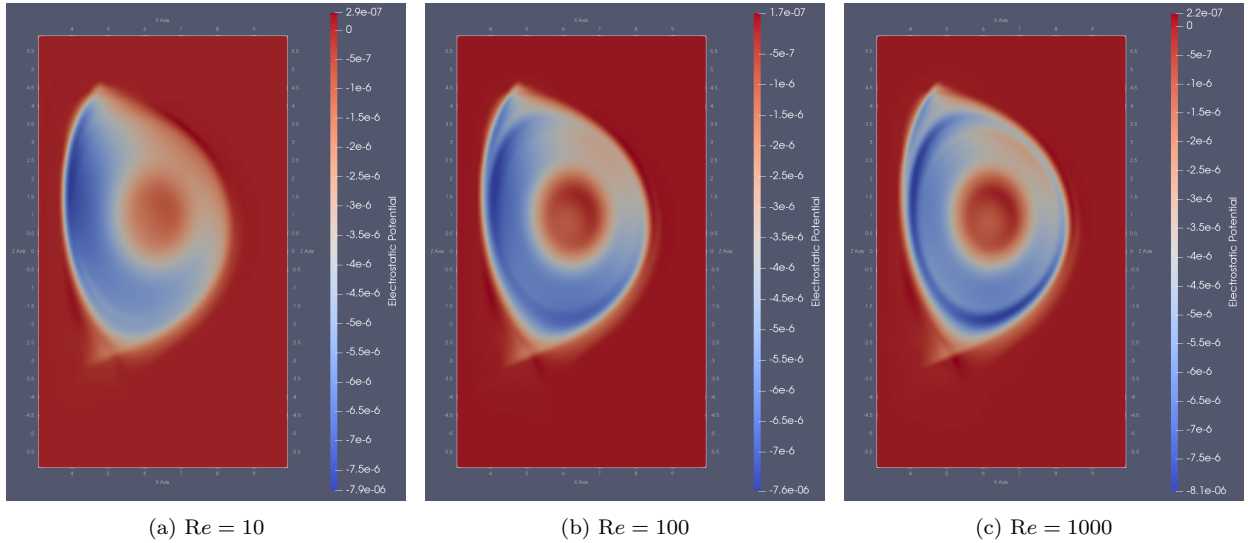


Figure 15: The electrostatic potential with different artificial viscosity coefficients at the first time step.

upward until it hits the rigid wall and the toroidal current in the plasma chamber gets almost entirely dissipated. The induced toroidal current in the vacuum vessel persists till the end of the simulation ( $t = 327.6$  ms), because the ITER vacuum vessel has a wall time that is longer (500 ms).

This example is further used to investigate the divergence-free property of the magnetic field of the MFD solver. Figure 20 depicts the evolution of the infinity norm of the divergence of the magnetic field over time. Figure 20b shows the non-normalized quantity whereas Figure 20a corresponds to the normalized one. Taking Figure 20a as an example, the initial divergence is not exactly zero but rather of the order of  $10^{-10}$ . Note that the initial condition is prepared through several steps as described in Section 5.2, which makes it difficult to get an exactly discrete divergence-free field, especially corresponding to the mimetic divergence operator. Nevertheless, as time evolves, the divergence fluctuates between two successive time steps by  $\pm 10^{-15}$ , which confirms

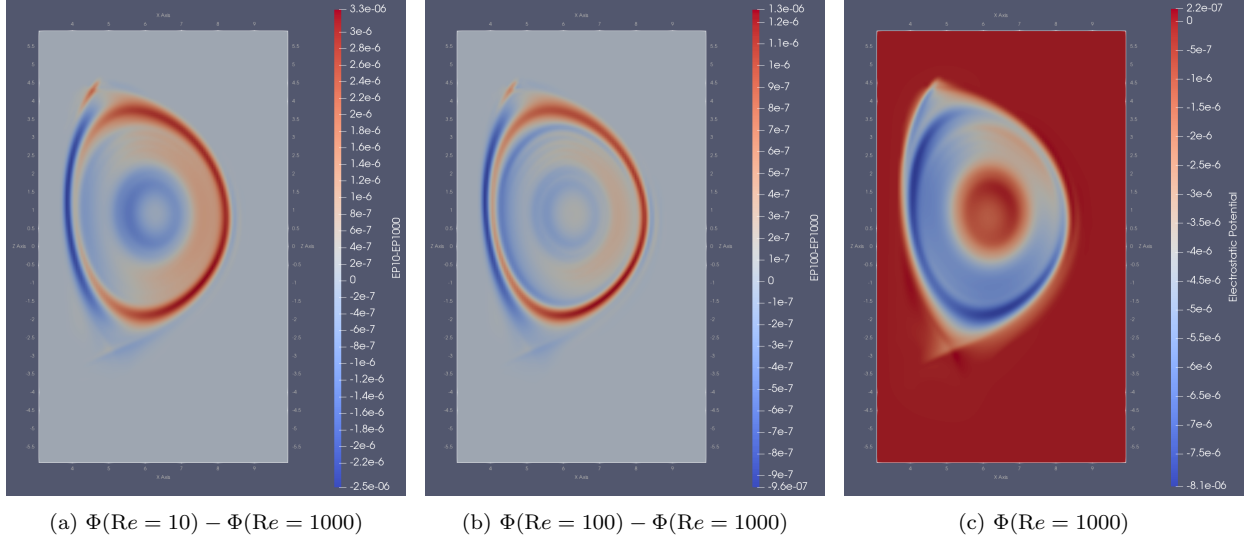


Figure 16: The electrostatic potential for  $\text{Re} = 1000$  and the differences  $\Phi(\text{Re} = 100) - \Phi(\text{Re} = 1000)$  and  $\Phi(\text{Re} = 10) - \Phi(\text{Re} = 1000)$  at the first time step.

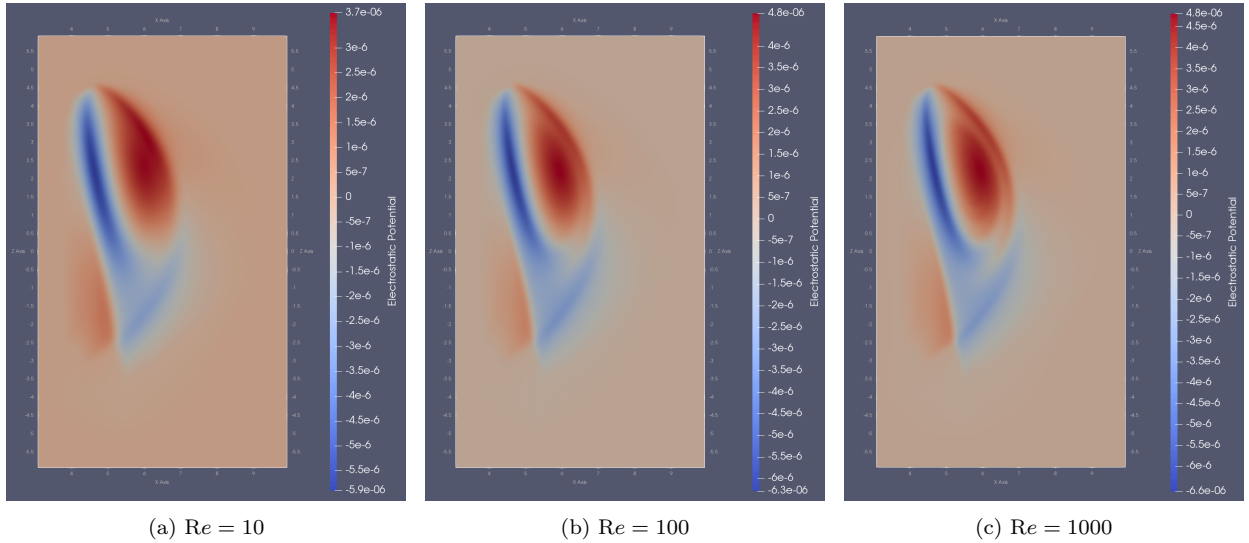


Figure 17: The electrostatic potential with different artificial viscosity coefficients after 50 time steps.

the divergence-free property of the magnetic field as stated in Section 3.2. Here the fluctuation is due to an iterative nonlinear solver being used. Nevertheless, such a small error is more than enough for the tests considered here for avoiding any potential numerical artifacts due to the divergence error.

#### 5.4.2. Anisotropic setting

Lastly, we provide the results of a full ITER VDE simulation for the case of anisotropic resistivity at the first wall and blanket module (see Formulas (34) and (35) in Section 2.2) and a fictitious viscosity regularization term with  $\text{Re} = 100$ . The resistivity values tested are as follows:

- $\eta = 1.71 \times 10^{-5} \Omega \text{ m}$  in the plasma chamber (that corresponds to an electron temperature of  $T_e = 10\text{eV}$ );

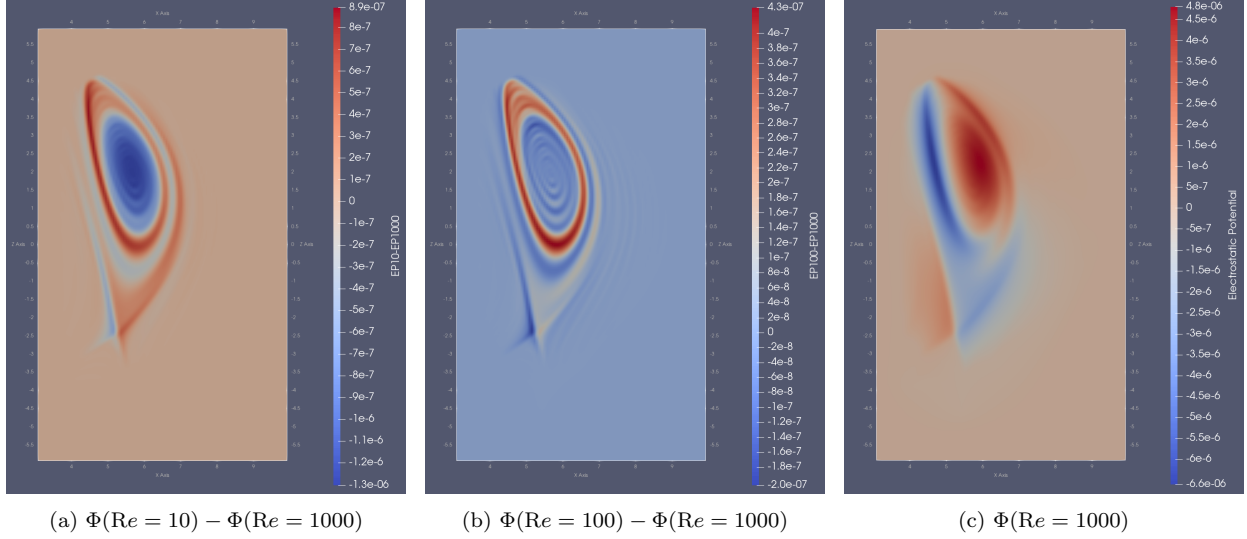


Figure 18: The electrostatic potential for  $\text{Re} = 1000$  and the differences  $\Phi(\text{Re} = 100) - \Phi(\text{Re} = 1000)$  and  $\Phi(\text{Re} = 10) - \Phi(\text{Re} = 1000)$  after 50 time steps.

- $\eta_t = 4.4 \times 10^{-2} \Omega \cdot \text{m}$  in the blanket module;
- $\eta_p = 1.71 \times 10^{-5} \Omega \cdot \text{m}$  in the blanket module;
- $\eta = 1.3 \times 10^{-6} \Omega \text{m}$  in the vacuum vessel;
- $\eta = 1.3 \times 10^{-3} \Omega \text{m}$  in the region outside the wall.

The so called “halo currents” are illustrated in Figure 21 where the toroidal current is given by the colormap and the poloidal current is presented as streamlines. We observe that the toroidal current is eliminated and the halo current flows only poloidally in the blanket to enter the vacuum vessel, where the electrical current can have a strong toroidal component.

The electromagnetic force loading ( $\mathbf{j} \times \mathbf{B}$ ) due to the halo and eddy current in the blanket and vacuum vessel during a VDE can also be quantified from our simulation. The toroidal and poloidal components of the Lorentz force ( $\mathbf{j} \times \mathbf{B}$ ) are given in Figures 22 and 23 respectively, with the magnetic field lines at six different times of the simulation. We notice that the Lorentz force is initially concentrated along the plasma/wall interface whereas later in time, this force becomes stronger at the vacuum vessel and almost nil elsewhere.

### 5.5. Solver performance

In this section, we vary the resistivity value inside the plasma chamber and check the performance of the solver. More specifically, for each resistivity value, we examine the average numbers of nonlinear and linear iterations. The time step is fixed in each simulation, primarily depending on the plasma resistivity, such that it is always equal to 1% of the resistive diffusion time, i.e.,

$$\Delta t = 0.01 \tau_\eta = 0.01 \frac{a^2 \mu_0}{\eta},$$

where  $\mu_0$  denotes the permeability of free space and  $a$  is the minor radius which is considered to be equal to 2 for the ITER. We are interested in verifying that the performance of the solver is independent of  $\eta$ .

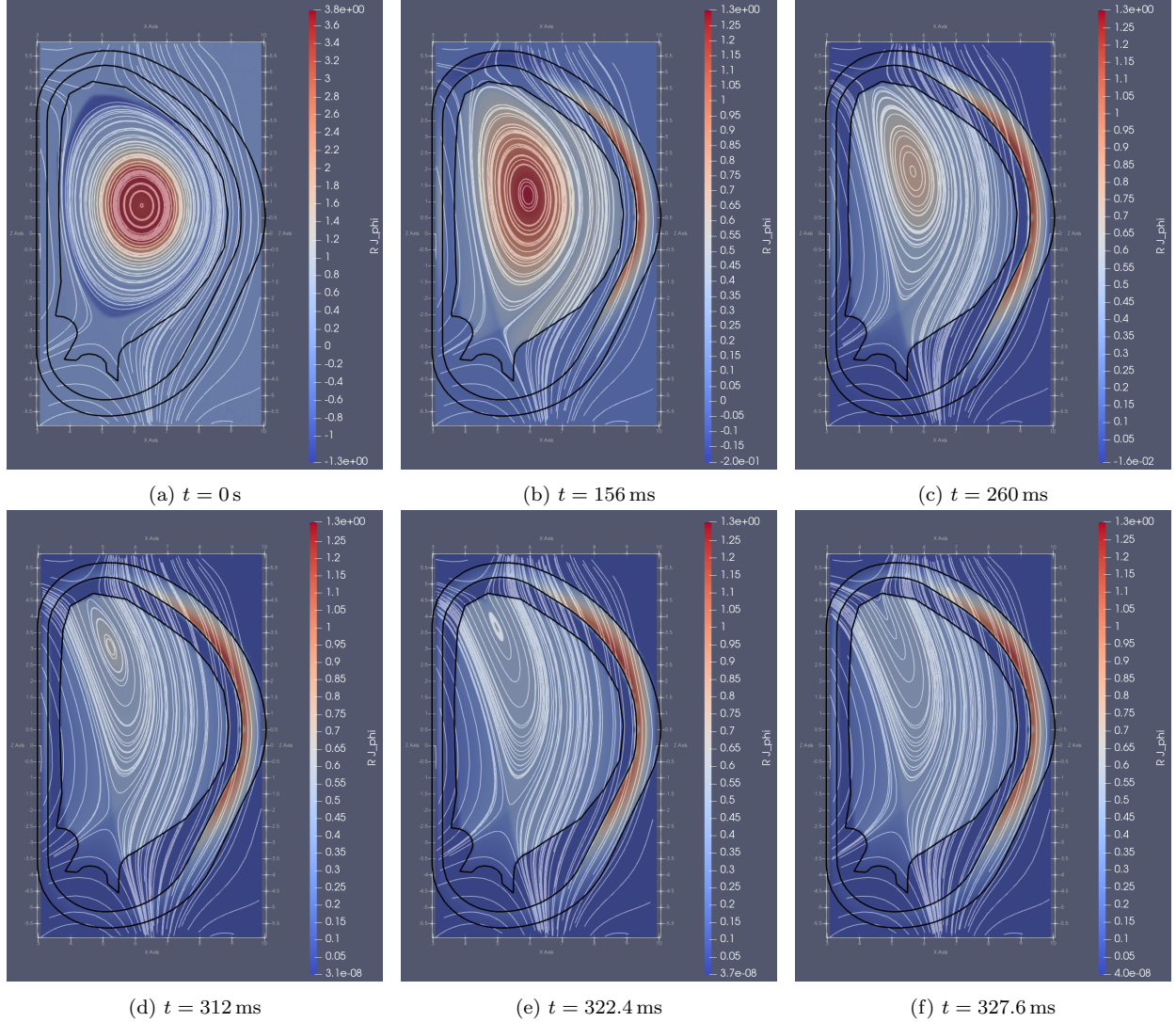


Figure 19: The toroidal current  $R(\nabla \times \mathbf{B})_\phi$  and streamlines of the poloidal magnetic field over time.

Table 1: Average number of iterations per time solve for full ITER VDE simulations with different plasma resistivities

$\eta$ ( $\Omega \text{ m}$ )	# of Newton its./solve	# of Krylov its./solve
$9.66 \times 10^{-6}$	3.98	10.94
$4.83 \times 10^{-6}$	3.98	12.14
$2.415 \times 10^{-6}$	4.03	12.98

We perform the simulations for 70 time steps and report the average numbers of linear and nonlinear iterations over the entire simulations in Table 1. It is found that the number of nonlinear iterations seems to be stable (around 4 iterations per solve) for the different plasma resistivity values tested, whereas the simulations with lower resistivities seem to be more computationally demanding on the algebraic level as the linear solver seems to require slightly more iterations. The increase remains at a reasonable level for the resistivity range tested though. The default restart value of GMRES in PETSc is 30, which is much larger than this iteration number. The algorithm performance confirms our preconditioning strategy is efficient. In the future work, we will further



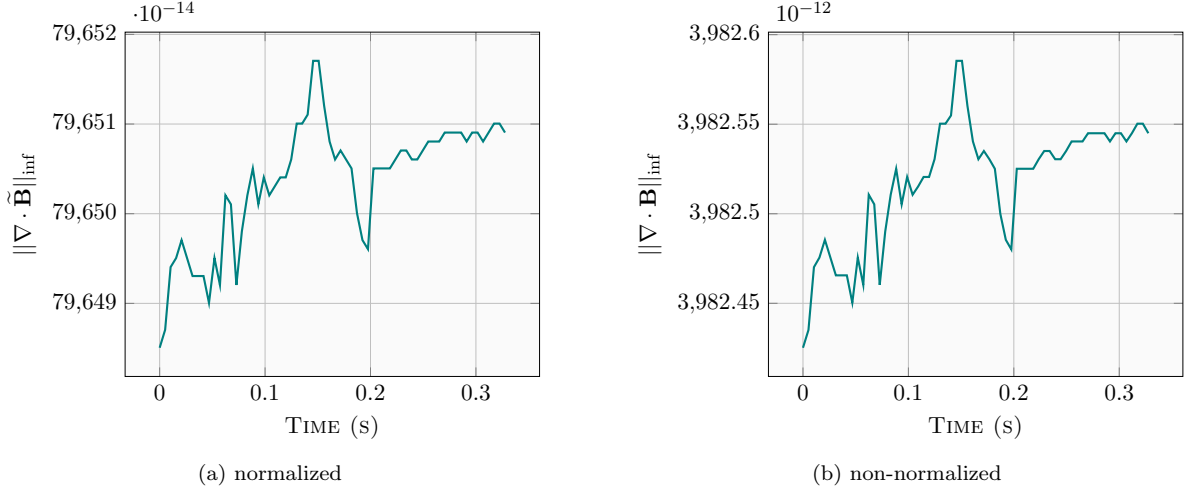


Figure 20: Evolution of the infinity norm of the divergence of the magnetic field over time.

improve the inner sub-block solver by replacing the direct solver for the  $\{\mathbf{V}, \mathbf{B}\}$  block with a more scalable option.

## 6. Conclusions

In this article, we presented a mimetic finite difference discretization of a regularized quasi-static perpendicular plasma dynamics model that is designed to preserve the divergence of the magnetic field. We also proposed a four-level block preconditioner where the factorization and solver strategy is exact for 2 blocks and the overall solver shows good performance. In addition, the properties of the mimetic operators help eliminate sub-blocks in the Schur complement in the third level of this preconditioner. The numerical results show that the fluctuations in the divergence remain within the machine precision range and that the performance of the nonlinear solver and the preconditioner allows large time steps for a range of Lundquist numbers. Lastly, the full VDE simulation over the actual plasma current diffusion time was shown for ITER configuration.

## Acknowledgement

We would like to thank the PETSc team for a number of helpful discussions. In particular, we thank Patrick Sanan, the primary developer of DMStag, for many useful discussions. This research used resources provided by the Los Alamos National Laboratory Institutional Computing Program, which is supported by the U.S. Department of Energy National Nuclear Security Administration under Contract No. 89233218CNA000001. This research also used resources of the National Energy Research Scientific Computing Center, which is supported by the Office of Science of the U.S. Department of Energy under Contract No. DE-AC02-05CH11231.

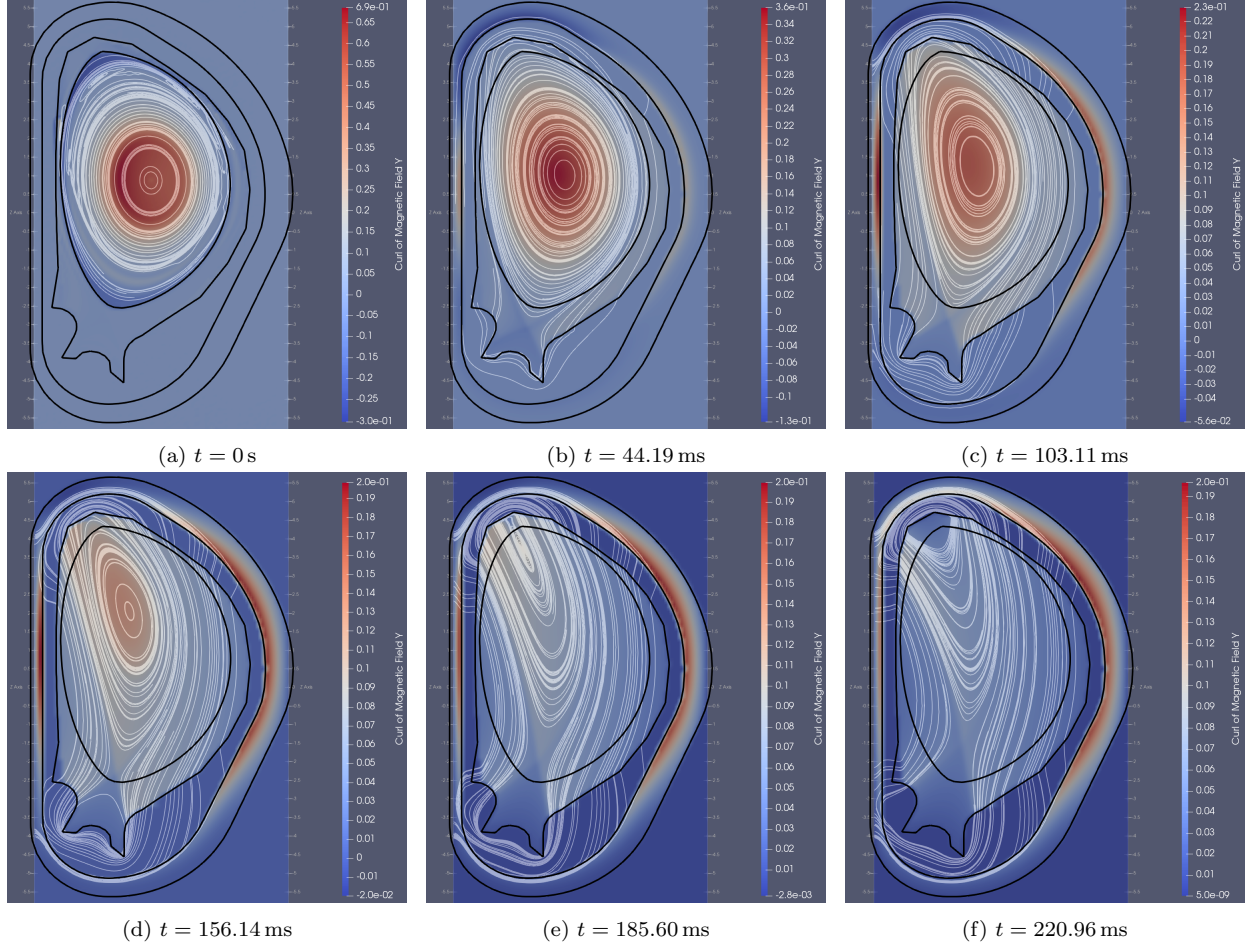


Figure 21: The toroidal current  $(\nabla \times \mathbf{B})_\phi$  and streamlines of the poloidal current  $(\nabla \times \mathbf{B})_{\text{pol}}$  over time. At  $t=103.11$  ms, a halo current (on the top left region in subfigure 21c) is observed to form.

## Appendix A. Nonuniqueness of solutions to the model without the viscosity term

This section addresses the nonuniqueness of the solution to the model without the viscosity regularization term. Consider the following model in a single domain

$$-\left(\frac{1}{\mu_0}(\nabla \times \mathbf{B}) \times \mathbf{B}\right) \cdot \mathbf{e}_R = 0 \quad \text{in } \Omega^W, \quad (\text{A.1})$$

$$\mathbf{V}_{i\perp} \cdot \mathbf{B} = 0 \quad \text{in } \Omega^W, \quad (\text{A.2})$$

$$-\left(\frac{1}{\mu_0}(\nabla \times \mathbf{B}) \times \mathbf{B}\right) \cdot \mathbf{e}_Z = 0 \quad \text{in } \Omega^W, \quad (\text{A.3})$$

$$\nabla^2 \Phi = -\nabla \cdot \left[ -\mathbf{V}_{i\perp} \times \mathbf{B} + \frac{\eta}{\mu_0} (\nabla \times \mathbf{B}) \right] \quad \text{in } \Omega^W, \quad (\text{A.4})$$

$$\boldsymbol{\tau} = \nabla \Phi - \mathbf{V}_{i\perp} \times \mathbf{B} + \frac{\eta}{\mu_0} (\nabla \times \mathbf{B}) \quad \text{in } \Omega^W, \quad (\text{A.5})$$

$$\frac{\partial \mathbf{B}}{\partial t} = -\nabla \times \boldsymbol{\tau} \quad \text{in } \Omega^W, \quad (\text{A.6})$$

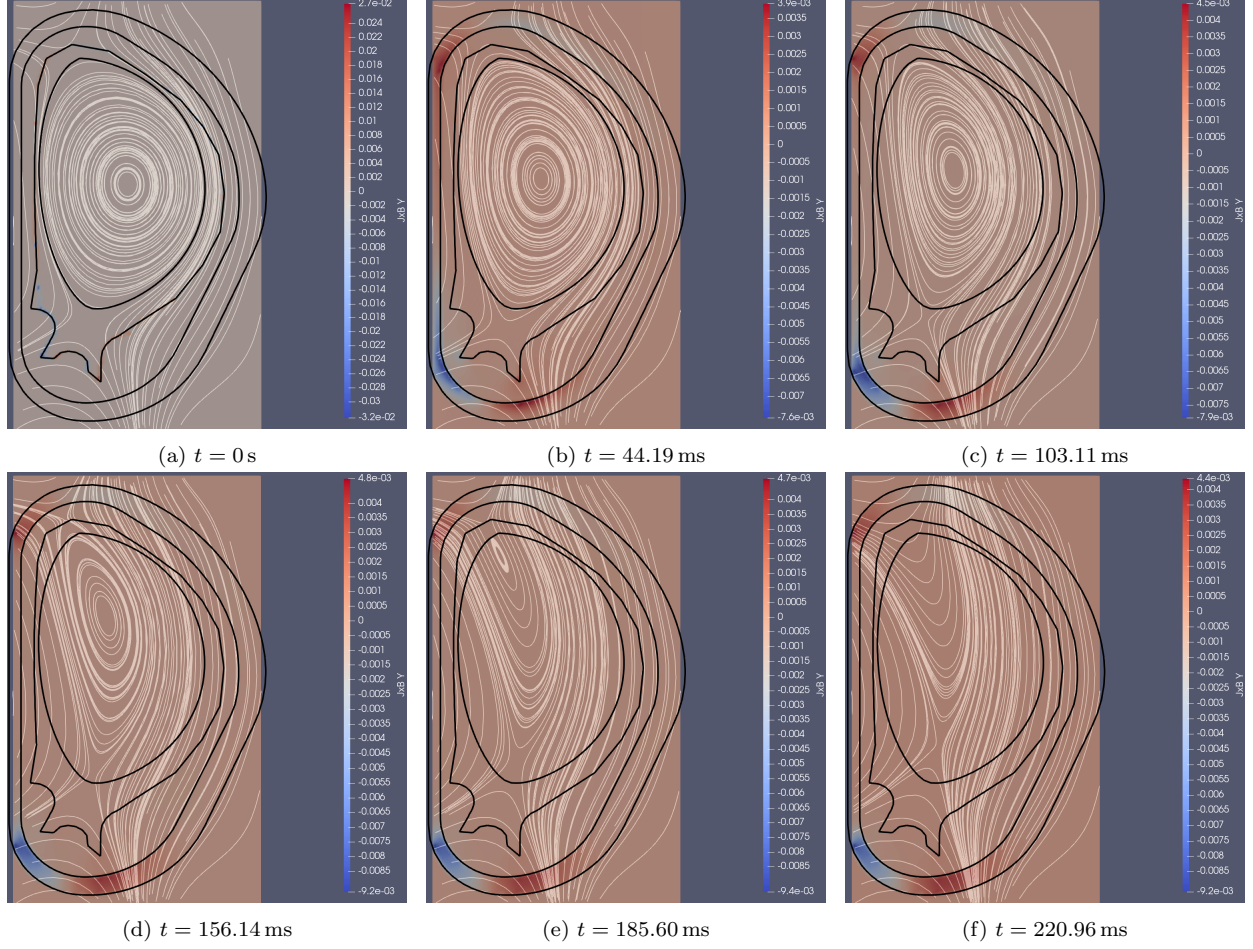


Figure 22: The toroidal component of the Lorentz Force  $((\nabla \times \mathbf{B}) \times \mathbf{B})_\phi$  and streamlines of the poloidal magnetic field over time.

under some proper boundary condition

$$\mathbf{V}_{i\perp} = \mathbf{0} \quad \text{on } \partial\Omega^W, \quad (\text{A.7})$$

$$\Phi = \Phi_{bc} \quad \text{on } \partial\Omega^W, \quad (\text{A.8})$$

$$\tau = \tau_{bc} \quad \text{on } \partial\Omega^W. \quad (\text{A.9})$$

The equation for  $n_i$  is dropped as it is not coupled to the four fields considered here. At first glance, it is tempting to assume the above system is well-posed since it is a closed system. We will however show the form of a possible null space that only needs to satisfy a mild constraint.

Let  $(\tau, \mathbf{B}, \mathbf{V}_{i\perp}, \Phi)$  and  $(\tau + \mathbf{Z}, \mathbf{B}, \mathbf{V}_{i\perp} + \mathbf{W}, \Phi + \varphi)$  be two solutions of the above system. We

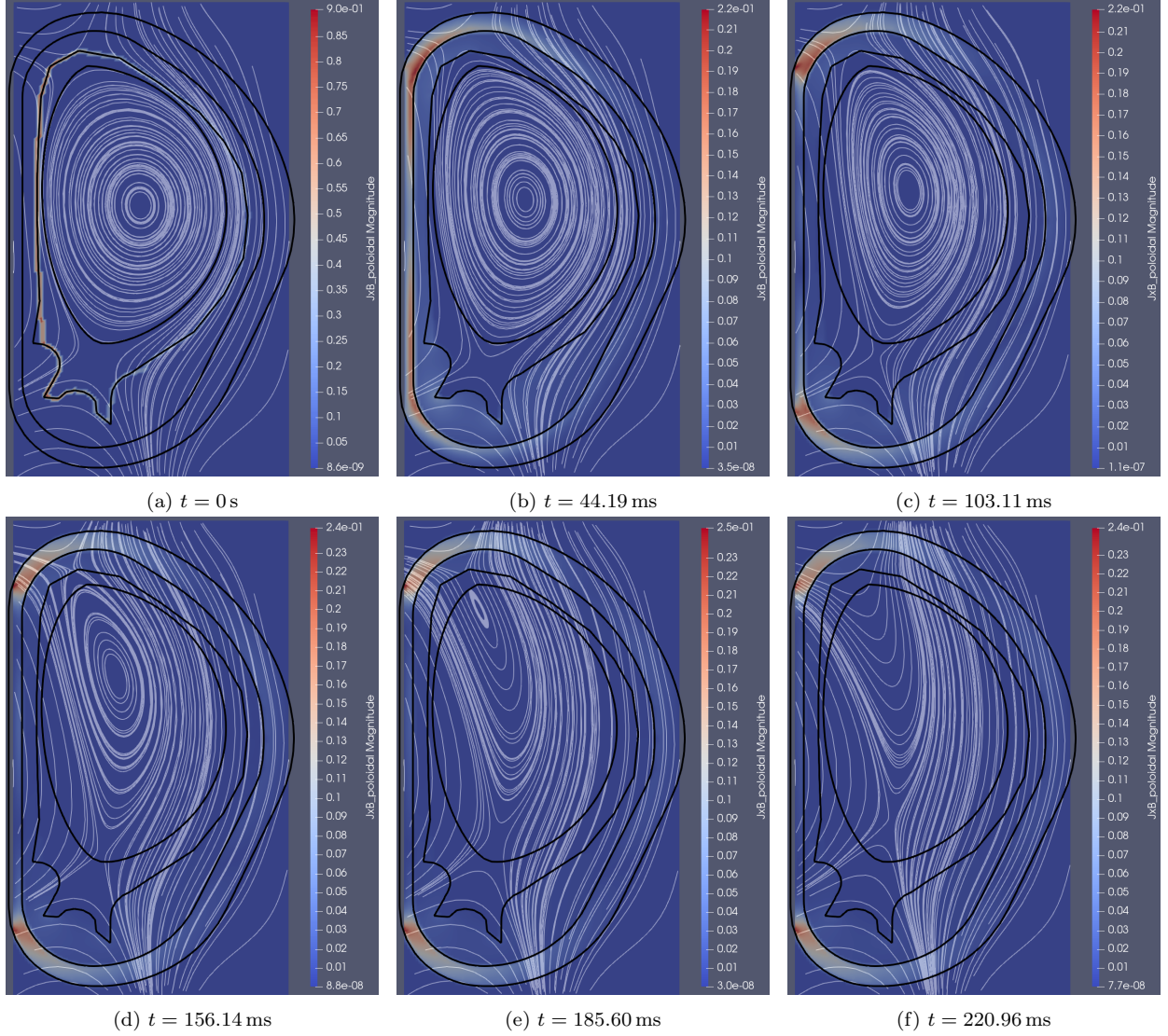


Figure 23: The magnitude of the poloidal component of the Lorentz Force  $\|((\nabla \times \mathbf{B}) \times \mathbf{B})_{\text{pol}}\|$  and streamlines of the poloidal magnetic field over time.

then have:

$$\mathbf{W} \cdot \mathbf{B} = 0 \quad \text{in } \Omega^W, \quad (\text{A.10})$$

$$\nabla^2 \varphi = \nabla \cdot (\mathbf{W} \times \mathbf{B}) \quad \text{in } \Omega^W, \quad (\text{A.11})$$

$$\mathbf{Z} = \nabla \varphi - \mathbf{W} \times \mathbf{B} \quad \text{in } \Omega^W, \quad (\text{A.12})$$

$$\nabla \times \mathbf{Z} = -\nabla \times (\mathbf{W} \times \mathbf{B}) = \mathbf{0} \quad \text{in } \Omega^W, \quad (\text{A.13})$$

$$\mathbf{W} = \mathbf{0} \quad \text{on } \partial\Omega^W, \quad (\text{A.14})$$

$$\varphi = 0 \quad \text{on } \partial\Omega^W, \quad (\text{A.15})$$

$$\mathbf{Z} = \mathbf{0} \quad \text{on } \partial\Omega^W. \quad (\text{A.16})$$

(A.13) implies that there exists a field  $g \in H^1(\Omega)$  such that:

$$\mathbf{W} \times \mathbf{B} = \nabla g; \quad (\text{A.17})$$

That further implies that

$$\nabla \cdot (\mathbf{W} \times \mathbf{B}) = \nabla^2 g = \nabla^2 \varphi. \quad (\text{A.18})$$

The Dirichlet boundary condition for  $\Phi$  suggests that  $g$  is equal to  $\varphi$ , and thus  $\nabla \varphi = \nabla g = \mathbf{W} \times \mathbf{B}$  and  $\mathbf{Z} = 0$ . Moreover, Equations (A.10) together with  $\nabla \varphi = \mathbf{W} \times \mathbf{B}$  are equivalent to:

$$\mathbf{W} = \|\mathbf{B}\|^{-2}(\mathbf{B} \times \nabla \varphi) \quad (\text{A.19})$$

$$\nabla \varphi \cdot \mathbf{B} = 0. \quad (\text{A.20})$$

To prove the equivalence  $\begin{cases} \mathbf{W} \cdot \mathbf{B} = 0 \\ \nabla \varphi = \mathbf{W} \times \mathbf{B} \end{cases} \Leftrightarrow \begin{cases} \mathbf{W} = \|\mathbf{B}\|^{-2}(\mathbf{B} \times \nabla \varphi) \\ \nabla \varphi \cdot \mathbf{B} = 0 \end{cases}$ , it suffices to compute the dot and cross product with  $\mathbf{B}$  for the bottom left side equation and the top right side equation. This identifies at least one null space for the system, which only needs the scalar function  $\varphi$  to satisfy the constraint (A.20). As pointed out in Section 2.1, such a constraint can be easily satisfied in the axisymmetric tokamak, as the magnetic field is given by (104) and any function of  $\varphi(\psi)$  satisfies (A.20).

## Appendix B. Regularization through the viscosity term

This section show the aforementioned null space is removed through the regularization term. For ease of presentation, we consider the full  $\mathbf{V}$  formulation. More specifically, we consider to replace the equations (A.1)–(A.3) with the following equation

$$\frac{1}{\mu_0}(\nabla \times \mathbf{B}) \times \mathbf{B} = -\nu n_0 m_i \nabla^2 \mathbf{V}. \quad (\text{B.1})$$

Let  $(\boldsymbol{\tau}, \mathbf{B}, \mathbf{V}, \Phi)$  and  $(\boldsymbol{\tau} + \mathbf{Z}, \mathbf{B}, \mathbf{V} + \mathbf{W}, \Phi + \varphi)$  again be two solutions of the new model. We then have:

$$\nabla^2 \mathbf{W} = \mathbf{0}, \quad (\text{B.2})$$

$$\nabla^2 \varphi = \nabla \cdot (\mathbf{W} \times \mathbf{B}), \quad (\text{B.3})$$

$$\mathbf{Z} = \nabla \varphi - \mathbf{W} \times \mathbf{B}, \quad (\text{B.4})$$

$$\nabla \times \mathbf{Z} = -\nabla \times (\mathbf{W} \times \mathbf{B}) = \mathbf{0}. \quad (\text{B.5})$$

The Dirichlet boundary condition implies that  $\mathbf{W} = 0$ ,  $\varphi = 0$ , and  $\mathbf{Z} = 0$ . Hence, we show the regularization term removes the null space. This analysis can be easily extended to the case with the  $\mathbf{V}_\perp$  case when we consider the axisymmetric case (i.e.,  $\partial/\partial\phi = 0$ ).

## Appendix C. Matrix definition of the derived mimetic operators

To obtain a matrix form of the dual operators, we note that inner products are represented by symmetric positive definite mass matrices:  $\mathbb{M}_n$  for  $\mathcal{N}_h$ ,  $\mathbb{M}_e$  for  $\mathcal{E}_h$ ,  $\mathbb{M}_f$  for  $\mathcal{F}_h$  and  $\mathbb{M}_c$  for  $\mathcal{C}_h$ . Hence,

$$(\mathbb{M}_e \text{Grad}_h p_h)^T \mathbf{v}_h = -(\mathbb{M}_n p_h)^T \widetilde{\text{Div}}_h \mathbf{v}_h,$$

$$(\mathbb{M}_c \text{Div}_h \mathbf{u}_h)^T p_h = -(\mathbb{M}_f \mathbf{u}_h)^T \widetilde{\text{Grad}}_h p_h,$$

$$(\mathbb{M}_f \text{Curl}_h \mathbf{u}_h)^T \mathbf{v}_h = (\mathbb{M}_e \mathbf{u}_h)^T \widetilde{\text{Curl}}_h \mathbf{v}_h.$$

These should hold true for any vectors  $p_h$ ,  $u_h$  and  $\mathbf{v}_h$ . As a consequence, the matrix definitions are given by

$$\widetilde{\text{Div}}_h = -\mathbb{M}_n^{-1} (\text{Grad}_h)^T \mathbb{M}_e, \quad (\text{C.1})$$

$$\widetilde{\text{Grad}}_h = -\mathbb{M}_f^{-1} (\text{Div}_h)^T \mathbb{M}_c, \quad (\text{C.2})$$

$$\widetilde{\text{Curl}}_h = \mathbb{M}_e^{-1} (\text{Curl}_h)^T \mathbb{M}_f. \quad (\text{C.3})$$

The mass matrices are diagonal on structured meshes that are considered in the current work.

To discretize PDEs, the MFD framework builds upon three primary and three dual operators. The four discrete spaces along with their primary or derived operators form a discrete de Rham complex. The coefficients of the PDEs are usually embedded in the definition of the derived operator. Consider, for example, the following formulas:

$$\int_{\Omega} p \nabla \cdot \mathbf{u} \, dV = - \int_{\Omega} K^{-1} (K \nabla p) \cdot \mathbf{u} \, dV + \oint_{\partial\Omega} p (\mathbf{u} \cdot \mathbf{n}) \, dS, \quad (\text{C.4})$$

$$\int_{\Omega} \mathbf{u} \cdot (\nabla \times \mathbf{v}) \, dV = \int_{\Omega} K^{-1} (K \nabla \times \mathbf{u}) \cdot \mathbf{v} \, dV + \oint_{\partial\Omega} (\mathbf{u} \times \mathbf{v}) \cdot \mathbf{n} \, dS, \quad (\text{C.5})$$

where  $K$  is a positive definite tensor. These formulas represents the duality between the two first operators,  $\text{div}$  and  $(K \text{ grad})$  for the first equation,  $\text{curl}$  and  $(K \text{ curl})$  for the second one, using a weighted inner product for the vector fields (with  $K^{-1}$  as the weight). The corresponding discrete operators will be in a duality relation with respect to such an inner product.

## Appendix D. Magnetic energy dissipation

In this section, we show that with a viscosity term and under a proper boundary condition, an energy dissipation law can be achieved if we consider the total magnetic energy. Let  $(n_i, \boldsymbol{\tau}, \mathbf{B}, \mathbf{V}, \Phi)$  be the solution for the five-field model (with full  $\mathbf{V}$ ) with the viscosity term. The total magnetic energy is given by

$$E_{\mathbf{B}} := \frac{1}{2\mu_0} |\mathbf{B}|^2. \quad (\text{D.1})$$

We then have:

$$\frac{dE_{\mathbf{B}}}{dt} = \int_{\Omega} \frac{1}{\mu_0} \left( \mathbf{B} \cdot \frac{\partial \mathbf{B}}{\partial t} \right) dV, \quad (\text{D.2})$$

$$= -\frac{1}{\mu_0} \int_{\Omega} (\mathbf{B} \cdot (\nabla \times \boldsymbol{\tau})) dV, \quad (\text{D.3})$$

$$= -\frac{1}{\mu_0} \int_{\Omega} (\boldsymbol{\tau} \cdot (\nabla \times \mathbf{B})) dV - \oint_{\partial\Omega} (\mathbf{B} \times \boldsymbol{\tau}) \cdot \mathbf{n} dS, \quad (\text{D.4})$$

$$= -\frac{1}{\mu_0} \int_{\Omega} \left( (-\mathbf{V} \times \mathbf{B} + \frac{\eta}{\mu_0} \nabla \times \mathbf{B}) \cdot (\nabla \times \mathbf{B}) \right) dV, \quad (\text{D.5})$$

$$= \frac{1}{\mu_0} \int_{\Omega} ((\mathbf{V} \times \mathbf{B}) \cdot (\nabla \times \mathbf{B})) dV - \frac{1}{\mu_0^2} \int_{\Omega} \eta |\nabla \times \mathbf{B}|^2 dV, \quad (\text{D.6})$$

$$= -\frac{1}{\mu_0} \int_{\Omega} ((\nabla \times \mathbf{B}) \times \mathbf{B}) \cdot \mathbf{V} dV - \frac{1}{\mu_0^2} \int_{\Omega} \eta |\nabla \times \mathbf{B}|^2 dV, \quad (\text{D.7})$$

$$= \nu n_0 m_i \int_{\Omega} (\mathbf{V} \cdot \nabla^2 \mathbf{V}) dV - \frac{1}{\mu_0^2} \int_{\Omega} \eta |\nabla \times \mathbf{B}|^2 dV, \quad (\text{D.8})$$

$$= -\nu n_0 m_i \int_{\Omega} |\nabla \mathbf{V}|^2 dV + \nu n_0 m_i \oint_{\partial\Omega} (\mathbf{V} \cdot (\nabla \mathbf{V} \cdot \mathbf{n})) dS - \frac{1}{\mu_0^2} \int_{\Omega} \eta |\nabla \times \mathbf{B}|^2 dV, \quad (\text{D.9})$$

$$= -\nu n_0 m_i \int_{\Omega} |\nabla \mathbf{V}|^2 dV - \frac{1}{\mu_0^2} \int_{\Omega} \eta |\nabla \times \mathbf{B}|^2 dV, \quad (\text{D.10})$$

$$\leq 0. \quad (\text{D.11})$$

Here we drop the boundary integral terms assuming the proper boundary condition is imposed.

## References

- [1] J. P. H. Goedbloed, S. Poedts, Principles of Magnetohydrodynamics, Cambridge University Press, Cambridge, UK, 2004.
- [2] S. Chandrasekhar, P. C. Kendall, On force-free magnetic fields, *Astrophysical J.* 126 (1957) 457.
- [3] A. H. Boozer, Physics of magnetically confined plasmas, *Rev. Mod. Phys.* 76 (2004) 1071.
- [4] L. Woltjer, A theorem on force-free magnetic fields, *Proc. Natl. Acad. Sci. USA* 44 (1958) 489.
- [5] J. B. Taylor, Relaxation of toroidal plasma and generation of reverse magnetic fields, *Phys. Rev. Lett.* 33 (1974) 1139.
- [6] J. B. Taylor, Relaxation and magnetic reconnection in plasmas, *Rev. Mod. Phys.* 58 (1986) 741.
- [7] X. Z. Tang, A. H. Boozer, Current drive by co-axial helicity injection in a spherical torus, *Phys. Plasmas* 11 (2004) 2679.
- [8] X. Z. Tang, A. H. Boozer, Equilibrium and resistive steady state of a co-axial helicity injection plasma, *Phys. Plasmas* 10 (2003) 3661.
- [9] D. Bonfiglio, M. Veranda, S. Cappello, D. F. Escande, L. Chacón, Experimental-like helical self-organization in reversed-field pinch modeling, *Phys. Rev. Lett.* 111 (2013) 085002.

- [10] X. Z. Tang, A. H. Boozer, Reactor prospect of spheromak concept by electrostatic helicity injection, *Phys. Plasmas* 15 (2008) 072510.
- [11] X. Z. Tang, A. H. Boozer, Flux amplification in helicity injected spherical tori, *Phys. Plasmas* 12 (2005) 042113.
- [12] X. Z. Tang, A. H. Boozer, Spherical tokamak with a plasma center column, *Phys. Plasmas* 13 (2006) 042514.
- [13] X. Z. Tang, A. H. Boozer, Scale-up of spherical tokamak solenoid-free startup by co-axial helicity injection, *Phys. Plasmas* 14 (2007) 100704.
- [14] V. A. Izzo, Dispersive shell pellet injection modeling and validation for diii-d disruption mitigation, *Physics of Plasmas* 28 (8) (2021) 082502.
- [15] T. Wiegmann, T. Sakurai, Solar force-free magnetic fields, *Living Reviews in Solar Physics* 9 (1) (2012) 5.
- [16] X. Z. Tang, Self-organization of radio lobe magnetic fields by driven relaxation, *Astrophysical Journal* 679 (2008) 1000–1017.
- [17] A. A. Pevtsov, R. C. Canfield, T. R. Metcalf, Patterns of Helicity in Solar Active Regions, *ApJ* 425 (1994) L117.
- [18] Régnier, S., Amari, T., Kersalé, E., 3d coronal magnetic field from vector magnetograms: non-constant-ce-free configuration of the active region noaa 8151, *A&A* 392 (3) (2002) 1119–1127.
- [19] M. L. DeRosa, C. J. Schrijver, G. Barnes, K. D. Leka, B. W. Lites, M. J. Aschwanden, T. Amari, A. Canou, J. M. McTiernan, S. Régnier, J. K. Thalmann, G. Valori, M. S. Wheatland, T. Wiegmann, M. C. M. Cheung, P. A. Conlon, M. Fuhrmann, B. Inhester, T. Tadesse, A critical assessment of nonlinear force-free field modeling of the solar corona for active region 10953, *The Astrophysical Journal* 696 (2) (2009) 1780.
- [20] G. Valori, L. M. Green, P. Démoulin, S. Vargas Domínguez, L. van Driel-Gesztelyi, A. Wallace, D. Baker, M. Fuhrmann, Nonlinear force-free extrapolation of emerging flux with a global twist and serpentine fine structures, *Solar Physics* 278 (1) (2012) 73–97.
- [21] X. Z. Tang, A. H. Boozer, Force-free magnetic relaxation in driven plasmas, *Phys. Rev. Lett.* 94 (2005) 225004.
- [22] X. Z. Tang, A. H. Boozer, Constrained resonance in magnetic self-organization, *Phys. Rev. Lett.* 95 (2005) 155002.
- [23] X. Z. Tang, Driven resonances in partially relaxed plasma, *Phys. Rev. Lett.* 98 (2007) 175001.
- [24] C. J. McDevitt, X.-Z. Tang, C. J. Fontes, P. Sharma, H.-K. Chung, The constraint of plasma power balance on runaway avoidance, *Nuclear Fusion* 63 (2) (2023) 024001.
- [25] E. R. Priest, *Solar magnetohydrodynamics*, Vol. 21, Springer Science & Business Media, 2012.
- [26] R. Chodura, A. Schlüter, A 3D code for MHD equilibrium and stability, *Journal of Computational Physics* 41 (1) (1981) 68–88.



- [27] Z. Mikic, A. N. McClymont, Deducing coronal magnetic fields from vector magnetograms, in: *Solar Active Region Evolution: Comparing Models with Observations*, Vol. 68, 1994, p. 225.
- [28] A. N. McClymont, L. Jiao, Z. Mikić, Problems and progress in computing three-dimensional coronal active region magnetic fields from boundary data, *Solar Physics* 174 (1) (1997) 191–218.
- [29] G. Roumeliotis, The “stress-and-relax” method for reconstructing the coronal magnetic field from vector magnetograph data, *The Astrophysical Journal* 473 (2) (1996) 1095.
- [30] Valori, G., Kliem, B., Keppens, R., Extrapolation of a nonlinear force-free field containing a highly twisted magnetic loop, *A&A* 433 (1) (2005) 335–347.
- [31] L. E. Zakharov, X. Li, Tokamak magneto-hydrodynamics and reference magnetic coordinates for simulations of plasma disruptions, *Physics of Plasmas* 22 (6) (2015) 062511.
- [32] D. I. Kiramov, B. N. Breizman, Force-free motion of a cold plasma during the current quench, *Physics of Plasmas* 25 (9) (2018) 092501.
- [33] R. A. Nicolaides, D.-Q. Wang, Convergence analysis of a covolume scheme for maxwell’s equations in three dimensions, *Math. Comput.* 67 (223) (1998) 947–963.
- [34] B. nan Jiang, J. Wu, L. Povinelli, The origin of spurious solutions in computational electromagnetics, *Journal of Computational Physics* 125 (1) (1996) 104–123.
- [35] D. S. Balsara, Divergence-free reconstruction of magnetic fields and weno schemes for magnetohydrodynamics, *Journal of Computational Physics* 228 (14) (2009) 5040–5056.
- [36] B. Cockburn, F. Li, C.-W. Shu, Locally divergence-free discontinuous galerkin methods for the maxwell equations, *Journal of Computational Physics* 194 (2) (2004) 588–610.
- [37] K. Hu, Y. Ma, J. Xu, Stable Finite Element Methods Preserving  $\nabla \cdot \vec{\mathbf{B}} = 0$  Exactly for MHD Models, *Numer. Math.* 135 (2) (2017) 371–396.
- [38] C. R. Evans, J. F. Hawley, Simulation of magnetohydrodynamic flows—a constrained transport method, *The Astrophysical Journal* 332 (1988) 659–677.
- [39] J. A. Rossmannith, An unstaggered, high-resolution constrained transport method for magnetohydrodynamic flows, *SIAM Journal on Scientific Computing* 28 (5) (2006) 1766–1797.
- [40] A. J. Christlieb, J. A. Rossmannith, Q. Tang, Finite difference weighted essentially non-oscillatory schemes with constrained transport for ideal magnetohydrodynamics, *Journal of Computational Physics* 268 (2014) 302–325.
- [41] A. J. Christlieb, X. Feng, D. C. Seal, Q. Tang, A high-order positivity-preserving single-stage single-step method for the ideal magnetohydrodynamic equations, *Journal of Computational Physics* 316 (2016) 218–242.
- [42] A. J. Christlieb, X. Feng, Y. Jiang, Q. Tang, A high-order finite difference weno scheme for ideal magnetohydrodynamics on curvilinear meshes, *SIAM Journal on Scientific Computing* 40 (4) (2018) A2631–A2666.
- [43] D. Schötzau, Mixed finite element methods for stationary incompressible magneto-hydrodynamics, *Numerische Mathematik* 96 (2004) 771–800.

- [44] L. Chacón, A non-staggered, conservative,  $\nabla \cdot \mathbf{b} = 0$ , finite-volume scheme for 3d implicit extended magnetohydrodynamics in curvilinear geometries, *Computer Physics Communications* 163 (3) (2004) 143–171.
- [45] C. Sovinec, A. Glasser, T. Gianakon, D. Barnes, R. Nebel, S. Kruger, D. Schnack, S. Plimpton, A. Tarditi, M. Chu, Nonlinear magnetohydrodynamics simulation using high-order finite elements, *Journal of Computational Physics* 195 (1) (2004) 355–386.
- [46] J. Shadid, R. Pawlowski, E. Cyr, R. Tuminaro, L. Chacón, P. Weber, Scalable implicit incompressible resistive mhd with stabilized fe and fully-coupled newton–krylov–amg, *Computer Methods in Applied Mechanics and Engineering* 304 (2016) 1–25.
- [47] S. Badia, R. Codina, R. Planas, On an unconditionally convergent stabilized finite element approximation of resistive magnetohydrodynamics, *Journal of Computational Physics* 234 (2013) 399–416.
- [48] Q. Tang, L. Chacón, T. V. Kolev, J. N. Shadid, X.-Z. Tang, An adaptive scalable fully implicit algorithm based on stabilized finite element for reduced visco-resistive mhd, *Journal of Computational Physics* 454 (2022) 110967.
- [49] E. Cyr, J. Shadid, R. Tuminaro, R. Pawlowski, L. Chacon, A new approximate block factorization preconditioner for two-dimensional incompressible (reduced) resistive mhd, *SIAM Journal on Scientific Computing* 35.
- [50] L. Chacón, An optimal, parallel, fully implicit newton–krylov solver for three-dimensional viscoresistive magnetohydrodynamics, *Physics of Plasmas* 15 (5) (2008) 056103.
- [51] S. Badia, A. F. Martín, R. Planas, Block recursive lu preconditioners for the thermally coupled incompressible inductionless mhd problem, *Journal of Computational Physics* 274 (2014) 562–591.
- [52] Y. Ma, K. Hu, X. Hu, J. Xu, Robust preconditioners for incompressible mhd models, *Journal of Computational Physics* 316.
- [53] K. Lipnikov, G. Manzini, M. Shashkov, Mimetic finite difference method, *Journal of Computational Physics* 257 (2014) 1163–1227, physics-compatible numerical methods.
- [54] F. Brezzi, K. Lipnikov, M. Shashkov, V. Simoncini, A new discretization methodology for diffusion problems on generalized polyhedral meshes, *Computer Methods in Applied Mechanics and Engineering* 196 (37) (2007) 3682–3692, special Issue Honoring the 80th Birthday of Professor Ivo Babuska.
- [55] A. Cangiani, G. Manzini, A. Russo, Convergence analysis of the mimetic finite difference method for elliptic problems, *SIAM Journal on Numerical Analysis* 47 (4) (2009) 2612–2637.
- [56] B. da Veiga, J. Droniou, G. Manzini, A unified approach for handling convection terms in finite volumes and mimetic discretization methods for elliptic problems, *IMA Journal of Numerical Analysis* 31 (4) (2010) 1357–1401.
- [57] L. Beirão Da Veiga, A mimetic discretization method for linear elasticity, *ESAIM: Mathematical Modelling and Numerical Analysis* 44 (2) (2010) 231–250.

- [58] L. Beirão da Veiga, V. Gyrya, K. Lipnikov, G. Manzini, Mimetic finite difference method for the stokes problem on polygonal meshes, *Journal of Computational Physics* 228 (19) (2009) 7215–7232.
- [59] K. Lipnikov, J. Moulton, D. Svyatskiy, A multilevel multiscale mimetic (m3) method for two-phase flows in porous media, *Journal of Computational Physics* 227 (14) (2008) 6727–6753.
- [60] L. Pareschi, G. Russo, Implicit–explicit runge–kutta schemes and applications to hyperbolic systems with relaxation, *Journal of Scientific Computing* 25 (2005) 129–155.
- [61] M. Benzi, G. H. Golub, J. Liesen, Numerical solution of saddle point problems, *Acta numerica* 14 (2005) 1–137.
- [62] P. Bochev, R. B. Lehoucq, On the finite element solution of the pure neumann problem, *SIAM review* 47 (1) (2005) 50–66.
- [63] M. Joshaghani, J. Chang, K. Nakshatrala, M. G. Knepley, Composable block solvers for the four-field double porosity/permeability model, *Journal of Computational Physics* 386 (2019) 428–466.
- [64] S. Balay, S. Abhyankar, M. F. Adams, S. Benson, J. Brown, P. Brune, K. Buschelman, E. M. Constantinescu, L. Dalcin, A. Dener, V. Eijkhout, W. D. Gropp, V. Hapla, T. Isaac, P. Jolivet, D. Karpeev, D. Kaushik, M. G. Knepley, F. Kong, S. Kruger, D. A. May, L. C. McInnes, R. T. Mills, L. Mitchell, T. Munson, J. E. Roman, K. Rupp, P. Sanan, J. Sarich, B. F. Smith, S. Zampini, H. Zhang, H. Zhang, J. Zhang, PETSc Web page, <https://petsc.org/> (2022).
- [65] S. Balay, S. Abhyankar, M. F. Adams, S. Benson, J. Brown, P. Brune, K. Buschelman, E. Constantinescu, L. Dalcin, A. Dener, V. Eijkhout, W. D. Gropp, V. Hapla, T. Isaac, P. Jolivet, D. Karpeev, D. Kaushik, M. G. Knepley, F. Kong, S. Kruger, D. A. May, L. C. McInnes, R. T. Mills, L. Mitchell, T. Munson, J. E. Roman, K. Rupp, P. Sanan, J. Sarich, B. F. Smith, S. Zampini, H. Zhang, H. Zhang, J. Zhang, PETSc/TAO users manual, Tech. Rep. ANL-21/39 - Revision 3.17, Argonne National Laboratory (2022).
- [66] S. Balay, W. D. Gropp, L. C. McInnes, B. F. Smith, Efficient management of parallelism in object oriented numerical software libraries, in: E. Arge, A. M. Bruaset, H. P. Langtangen (Eds.), *Modern Software Tools in Scientific Computing*, Birkhäuser Press, 1997, pp. 163–202.
- [67] S. Abhyankar, J. Brown, E. M. Constantinescu, D. Ghosh, B. F. Smith, H. Zhang, PETSc/TS: A modern scalable ODE/DAE solver library, Tech. rep. (2018).
- [68] P. Sanan, D. A. May, R. T. Mills, B. J. p. Kaus, Dmstag: Staggered, structured grids for petsc, *Journal of Open Source Software* 7 (79) (2022) 4531.
- [69] S. Liu, Q. Tang, X.-z. Tang, A parallel cut-cell algorithm for the free-boundary grad–shafranov problem, *SIAM Journal on Scientific Computing* 43 (6) (2021) B1198–B1225.